Journal of Fluids and Structures (1997) **11,** 793–817

SYMMETRIC AND ASYMMETRIC SEPARATION PATTERNS OVER A HEMISPHERE CYLINDER AT LOW REYNOLDS NUMBERS AND HIGH INCIDENCES

N. T. Hoang[†], O. K. Rediniotis[‡], and D. P. Telionis

Department of Engineering Science and Mechanics, Virginia Polytechnic Institute and State University, Blacksburg, VA 24061-0219, U.S.A.

(Received 29 January 1996 and in revised form 22 June 1997)

A careful documentation of the development of leeward vortices, horn vortices and separation bubbles over a hemisphere-cylinder is presented. Flow visualization, static pressure measurements and seven-hole-probe velocity measurements were obtained to provide a comprehensive picture of the flow at angles of attack $\alpha = 0$ to 45°. Skin-friction line topographies and static pressure data are presented. The results indicate that the development of the leeward vortices is strongly affected by the nose structures. Small disturbances on the nose result in steady wake asymmetries.

1. INTRODUCTION

Flows over bodies of revolution at incidence have received considerable attention in the last few decades. A number of careful investigations, both experimental and numerical, have been carried out. The basic fluid mechanics issues of interest are the development of three-dimensional separation, the formation of leeward vortices, the characteristics of natural unsteadiness around regions of separation and the development of steady asymmetric wakes. Early experimental efforts on flows over axisymmetric bodies were inspired by the theoretical arguments on "open" and "closed" separation (Maskell 1955; Wang 1975; Hsieh & Wang 1976). Historically, the prolate spheroid emerged first as an appropriate configuration for three-dimensional studies of flow separation. Patel & Baek (1983), Ericsson & Redding (1986) and Hoang *et al.* (1990) provide long lists of references on the topic. Flow-diagnostics techniques included surface flow visualization (Han & Patel 1974; Costis *et al.* 1989), surface static pressure measurements, three-hole probe measurements, and hot-film or hot-wire measurements (Hsieh 1977a, b, c; Meier & Kreplin 1980; Kreplin *et al.* 1982; Ramaprian *et al.* 1981). The effects of transition on the development of flow separation were also examined in these studies. Experimentalists moved further to document the development of vortex sheets which roll over axisymmetric bodies to form a pair of leeward vortices. These were achieved by hot-wire anemometers (Barber & Simpson 1991), surface hot-film sensors (Meier & Kreplin 1980; Kreplin *et al.* 1982) and laser-Doppler

---

[†] Present address: Aurora Flight Sciences Corporation, 9950 Wakeman Dr., Manassas, VA 22111, U.S.A.

[‡] Present address: Aerospace Engineering Department, Texas A&M University, College Station, TX 77843-3141, U.S.A.

0889-9746/97/070793 + 25 $25.00/fl970106

velocimetry (Hsieh, 1977b; Telionis & Costis 1983; Costis *et al.* 1989). A unique method of using a miniature fibre-optic LDV probe mounted inside a model to measure boundary-layer profiles (Chesnakas & Simpson 1994) has also been employed. The laser beams were directed through optical quality transparent windows.

Another sequence of investigations was motivated by the intricate topology of skin friction lines and their relationship to the flow patterns that develop above the surface of a body. Research conducted on this problem up to 1982 was reviewed by Tobak & Peake (1982) and Peake & Tobak (1982). These efforts were followed by contributions of Meade & Schiff (1987) Ying *et al.* (1986, 1987), Wang & Hsieh (1992) and Hsieh & Wang (1996).

The flow over a hemisphere-cylinder has been the subject of only a few experimental and computational investigations. A fundamental feature of the flow over a hemisphere-cylinder is nose separation which at small angles of attack appears in the form of a ring. This is usually a low-Reynolds-number effect and is the counterpart of laminar separation bubbles that develop in the leading edge of two-dimensional airfoils. In the three-dimensional case, these separated flow regions give rise to very complex configurations, prominent among which are the horn vortices. These are vortex filaments rooted near the nose of the model (Figure 1). Hsieh & Wang (1976) described this unique, tornado-like feature displayed by these vortices whose axes were conjectured to be normal to the solid surface.

Some authors refer to these vortices as "normal vortices" or Werlé vortices (Werlé 1962). Hsieh & Wang (1996) propose the term "tornado-like" vortices but we will refer to these structures here as "horn" vortices because of the compactness of this term. The flow over a prolate spheroid does not display any of these peculiar characteristics. All previous experimental work on hemisphere-cylinders was carried out in the transonic or the low supersonic regimes and were limited to angles of attack $\alpha = 0^\circ$ to $27{\cdot}5^\circ$. To the best of the authors' knowledge, data at low Reynolds numbers and low Mach numbers on such a model are currently not available. One of the purposes of this paper is to study the flow in this range of parameters and to examine the possible interaction of nose separation with the leeward vortices that dominate the wake of such models.

Hsieh (1975a, b, 1976, 1977a) employed surface oil flow, shadowgraphs, surface pressure measurements and laser-Doppler velocimetry measurements to study flow patterns over the hemisphere-cylinder at incidences from 0° to 1° in Mach number ranges from 0·6 to 1·5; the corresponding Reynolds number range was from $3{\cdot}4 \times 10^5$ to $8{\cdot}6 \times 10^5$, respectively, based on the diameter of the circular afterbody. Hsieh observed that at $\alpha = 0^\circ$, the existence of nose separation or separation bubble depended on the free-stream Mach number. At a Mach number $M_\infty = 0{\cdot}6$, the flow was well attached everywhere on the model. Between $M_\infty = 0{\cdot}7$ and 0·85, a separation bubble appeared and was most pronounced at $M_\infty = 0{\cdot}85$. Hsieh conjectured that no separation bubble exists for $M < 0{\cdot}6$. In the present experiments conducted at Mach numbers less than 0·2 and zero or small angles of attack, a nose bubble was actually always present. The Reynolds numbers were kept low enough to ensure laminar flow throughout.

At small angles of attack, a separation bubble near the nose wraps around the nose. If a model is given a moderate incidence, cross-flow causes the boundary layers to separate and roll up downstream to form a pair of leeward vortices as shown in Figure 1. Hsieh & Wang (1996) reserve the term "transverse" vortices for the leeward vortices, but this was employed to contrast with the term "normal" vortices they employed to denote horn vortices. As the incidence increases, the separation bubble gradually withdraws from the windside, while growing on the leeside. The size of the separation bubble depends on the Mach number, the Reynolds number and angle of attack. Nose separation and leeward

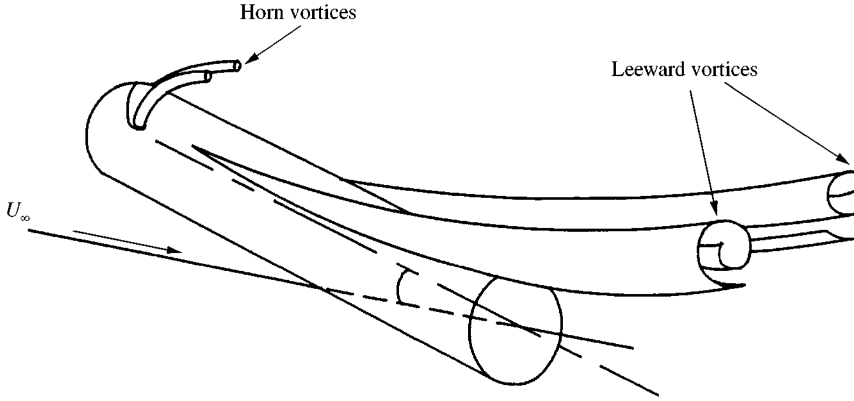

Figure 1. Leeward vortices and horn vortices over a hemisphere-cylinder at incidence.

vortices usually coexist. The nose bubble terminates at the horn vortices. At even higher incidences, although there were no data, Hsieh speculated that the separation bubble and the leeward vortices merge together to form a closed-type separation, and that then the horn vortices disappear. Hsieh & Wang (1996) most recently presented numerical evidence in support of this flow pattern. In the present paper we provide hard experimental data to document this behaviour.

There exist three types of separation lines on axisymmetric bodies: the nose separation line, the primary, and the secondary separation lines. The latter are commonly known as cross-flow separation. These are shown in Figure 2, which displays the topological structure proposed by Tobak & Peak (1979) for flow over a hemisphere-cylinder at an angle of attack of $\alpha = 10^\circ$. This is only a postulate and is presented here to familiarize the reader with the possible consistent patterns and terminology. Various nodes and saddle points in the pattern of skin-friction lines, marked by the symbols N and S, respectively, occur near the hemispherical nose. According to the accepted definition, the nose separation line is the line connecting S to N_1. The lines of primary and secondary separation are also marked in the figure. Tobak & Peak postulated that the line of primary separation originates from a saddle point of attachment (S_1) and a nodal point (N_3) on the windside of the model as shown in Figure 2. The vortex filament emerging from the focus (N_1) nearest to the plane symmetry can support a horn vortex and a dividing surface which extends the line of secondary separation into the flow.

Natural or forced vortex asymmetry patterns over a hemisphere-cylinder have not been documented experimentally in literature. Ying *et al.* (1987) demonstrated numerically the existence of vortex asymmetry over a hemisphere-cylinder model at 19° angle of attack and $M_\infty = 1{\cdot}2$ using the algorithm described in their 1986 paper. The present authors believe that there must be some sort of computational disturbance since no other computational or experimental evidence is available to support this finding. To date, there is no experimental evidence of asymmetric flow over blunt-nosed bodies at any incidence. Studies of asymmetric wakes, both numerical and experimental, were focused on the sharp-nosed models at low Reynolds numbers. There is a very long list of references on this topic and only a few recent contributions are cited here (Degani & Tobak 1991; Degani 1991; Keener & Chapman 1977; Moskovitz *et al.* 1989; Zilliac *et al.* 1990). But the physics of the two problems, flow

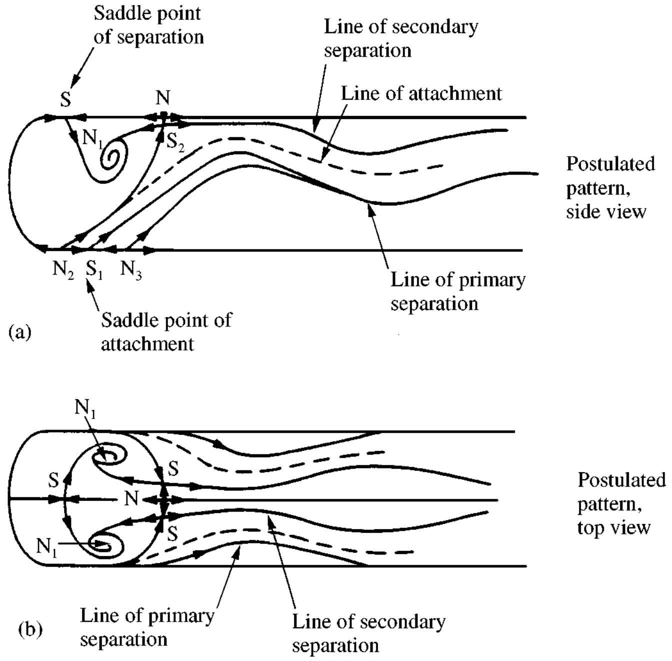

Figure 2. (a) Lines of separation and (b) topological structure for a flow over a hemisphere-cylinder at a moderate incidence from Tobak and Peak (1979).

over blunt-nosed and flow over sharp-nosed bodies, are significantly different. Separation over sharp-nosed axisymmetric configurations originates at the pointed nose. All separation patterns are open. Vortex asymmetry also originates at the nose. Moskovitz *et al.* (1989) investigated the effects of geometric perturbations on the asymmetric flow past an ogive/cone-cylinder. At angles of attack $\alpha > 30°$, they concluded that, with even minute disturbances, the flow was asymmetric. They also reported that discrete surface disturbances triggered the highest degree of asymmetry when located at a circumferential position near $\phi = 140°$. The effectiveness of the disturbance decreased with decrease in size and increase in distance from the model tip. In this paper we examine the influence of geometrical disturbances in the neighbourhood of the separation bubble on a hemisphere-cylinder. We demonstrate for the first time that very weak local disturbances can give rise to violent global deviations in the symmetry of the wake over a blunt-nosed body.

In a nutshell, we present here a comprehensive set of data to define carefully the role of nose separation in the development of the wake of a hemisphere-cylinder at low, medium and high angles of attack. Understanding of the complex patterns of pressure distributions and skin fraction lines may prove useful to numerical analysts who attempt to compute such flow fields.

2. EXPERIMENTAL SETUP

Two hemisphere-cylinder models were tested. The first was used for both flow visualization and velocity measurements. It consisted of a 1·65-inch-diameter hemisphere, followed by a cylindrical afterbody and was 13·5 in (343 mm) in length. The model could be shortened to

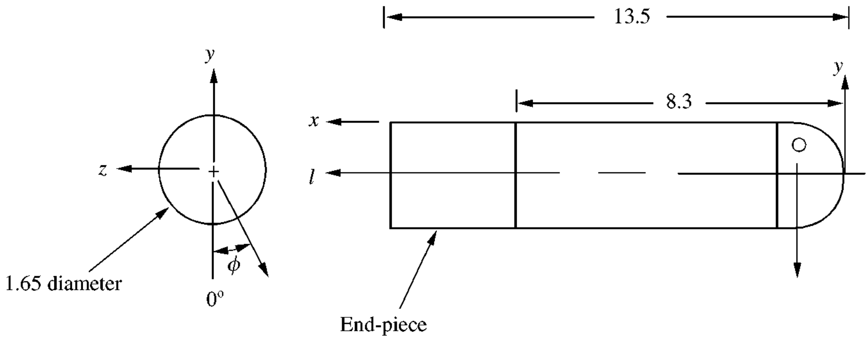

Figure 3. Coordinate system and schematic of the model. Dimensions (in inches; 1 in = 25.4 mm) correspond to one of the two models tested.

a length of 8·3 in (211 mm) by removing the end-piece. The surface was carefully sanded and coated with household furniture wax to reduce surface roughness. After each flow visualization run, the model was thoroughly washed with ethanol to remove stains from the flow visualization mixture. The model had to be repainted and rewaxed before each run.

The second model was used for static pressure measurements. Its overall length was 5·8 in (14·7 mm) and its diameter was 1·16 inches. This model was equipped with 32 pressure ports, each 1/32 in (0·79 mm) in diameter, along one of its meridionals. Figure 3 displays the definition of coordinates. The x-axis is measured along the periphery of the hemispherical cap in a meridional plane and then from the juncture of the hemisphere with the cylinder along a generator of the cylindrical afterbody. The y- and z-axes are normal to the free-stream velocity when the model is at zero incidence. The origin of the axes is located at the tip of the model and remains fixed to the body. Distances from the origin and along the axis of symmetry were designated by the symbol. To facilitate reliable measurements of the axial pressure gradient across the separation bubble, the pressure orifices were spaced closer to each other near the nose than over the afterbody. At each angle of attack, the model was rotated about its axis of symmetry to measure pressure at various cross-sectional stations. This yielded surface-pressure distributions constituting of 608 data points per incidence.

Tests were carried out in a 20 × 20 in (508 × 508 mm) wind tunnel (the ESM Wind Tunnel). The experimental rig is shown in Figure 4. A seven-hole probe was positioned parallel to the oncoming flow. The probe was traversed along a plane, normal to the free-stream velocity and 3 in (76 mm) away from the trailing-edge of the model. Velocity fields were mapped out on a 40-by-30 rectangular grid consisting of a total of 1200 points per plane. Each plane of data took approximately 16 continuous wind tunnel hours to complete. The free-stream velocity was continuously monitored and used to normalize all three velocity components. The mesh sizes, δy and δz, were equal to 0·1 in (2·54 mm).

The displacement of the seven-hole probe in the y- and z-direction was controlled by a Velmex UniSlide traversing table and a Microslide traversing table, respectively. The first was equipped with a stepping motor and a 8300 series Velmex indexer, resulting in translational resolution of 0·008 in (0·203 mm). The MicroSlide traversing table was equipped with a Compumotor Stepping Motor CXT 29-35 and a CX indexer/driver, with a resolution of 0·01 in (0·254 mm). Each indexer was capable of storing and executing complex motion programs from its own non-volatile memory (EPROM). A program,

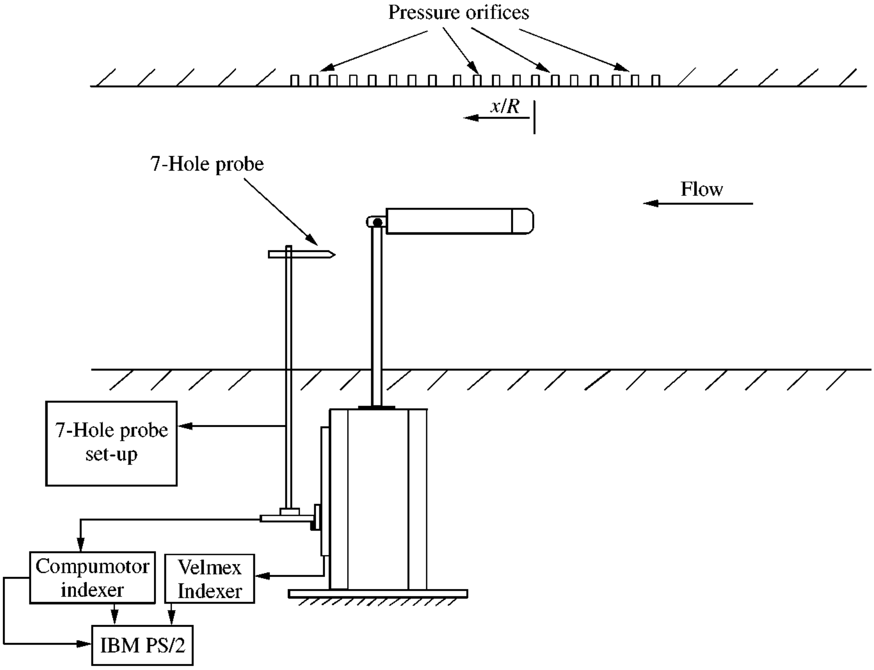

Figure 4. Seven-hole probe experimental setup.

written in Turbo Pascal and Inline Assembly Code, was downloaded to each indexer via an RS-232 interface from an IBM PS/2 computer to control the stepping motors.

Skin friction line visualizations were carried out at a free-stream velocity of 31·8 ft/s (9·69 m/s), corresponding to a Reynolds number of $\mathrm{Re} = 27\,000$. Before each run, a mixture of oleic acid, kerosene and titanium dioxide was painted on the model by a brush. The flow was sustained at a constant speed until the visualization mixture formed a steady-state skin friction pattern. After the completion of each test, the visualization mixture was dried flush with the surface of the model. The model was then removed from the sting and photographed. Photographs taken include three different views from $\phi = 90°$ (side view), $\phi = 120°$ (oblique view) and $\phi = 180°$ (leeward view). The angle of attack was varied from $\alpha = 0°$ to 45° in 5° increments.

Static pressure coefficients on the surface of a hemisphere-cylinder were obtained in the ESM Wind Tunnel at four angles of attack $\alpha = 0°$, 10°, 20°, and 30°. Data were taken along the x-axis from $\phi = 0°$ to 180° in 10° increments. To examine deviations between results obtained under two different turbulence levels and blockage conditions, some tests were performed in the VPI Stability Wind Tunnel at $\alpha = 20°$ at exactly the same conditions. The ESM Wind Tunnel wall pressure distributions were also measured, with the model placed at various incidences, to investigate the effect of the tunnel walls. All model wall pressure measurements were conducted at free-stream velocities of 25·9 ft/s (7·89 m/s) and 45·2 ft/s (13·8 m/s) corresponding to Reynolds numbers o $\mathrm{Re} = 1{\cdot}5 \times 10^4$ and $2{\cdot}7 \times 10^4$, respectively. The Reynolds numbers were based on the diameter of the circular afterbody. Pressure data presented here represent only half of the model surface. It was not necessary to obtain data for the entire surface of the model since the flow was symmetric for all values of α, as shown by flow visualization. No smoothing schemes were applied to the raw pressure data.

Velocity fields in the wake of a hemisphere-cylinder were obtained in the ESM Wind Tunnel at angles of attack $\alpha = 20^\circ$ and 30° and a Reynolds number of $2{\cdot}7 \times 10^4$ to confirm that the leeward vortices are symmetric. Data were also obtained with models equipped with a bead on the nose, to trigger asymmetric wakes. All velocity measurements were taken in a plane normal to the free-stream velocity, downstream of the model, using a seven-hole probe. Nondimensional axial vorticity was calculated via the equation

$$\Omega = \frac{D}{U_\infty}\left(\frac{\partial v}{\partial z} - \frac{\partial w}{\partial y}\right),$$

where D is the diameter of the cylindrical afterbody and U_∞ is the free-stream velocity. Calculated vorticity fields were smoothed using the International Mathematics Subroutine Library (IMSL) routine DCSSMH. This routine returns a cubic spline approximation to the data. The vorticity fields were then plotted to determine the effectiveness of the bead size and location.

3. RESULTS & DISCUSSION

3.1. Flow Visualization

A large number of flow visualizations were obtained and are included in Hoang (1991). Here we present only the most characteristic frames which expose a specific feature of the flow. At zero incidence, the separation bubble forms two complete rings around the model: a separation ring at about $x/R = 1{\cdot}5$ and a reattachment ring at $x/R = 2{\cdot}4$. This is not shown here due to lack of space. The fluid inside the bubble is trapped and the fluid outside originates far upstream. This type of flow is known as closed or bubble separation (Maskell 1995; Wang 1975). Very-slow-moving fluid exists inside the bubble. Consequently, the original paintbrush marks within this region did not change after the model was placed in the flow. Hsieh (1977) reported that for Mach numbers under 0·6, no nose bubble exits at $\alpha = 0^\circ$. His data, however, were obtained at a Reynolds number 10 times greater than the present.

At 5° incidence (again, not shown here), the separation bubble is no longer axisymmetric. Part of the reattachment ring on the windside moves forward, resulting in a gradual decrease in the width of the bubble from the leeward to the windward side. An interesting detail occurs on the flank of the model where the reattachment ring smears over an area from approximately $\phi = 10^\circ$ to 100° at $x/R = 1{\cdot}6$. This indicates a fuzzy separation between attached and separated flow. This phenomenon is observed only during transition from closed to open separation. Leeward vortices have not yet appeared, a fact that will be confirmed later with static pressure data. The existence of horn vortices is also not detected at this angle of attack. Similar to the zero-degree-incidence case, the flow exhibits closed separation.

Figures 5(a), 5(b), and 5(c) show three different views, $\phi = 180^\circ$, 120°, and 90°, respectively, of the hemisphere-cylinder at 10° incidence. In contrast to smaller angles of attack tested, the bubble width reaches a minimum at $\phi = \pm 80^\circ$ and grows somewhat as ϕ approaches 0°. Small isolated nearly-circular patches of dye along the periphery of the line of reattachment indicate the presence of horn vortices. These are areas where the visualization dye accumulates, collecting from the surrounding surface. The two horn vortices appear in the vicinity of $\phi = \pm 150^\circ$ and $x/R = 2.1$. The pattern is not entirely consistent with the

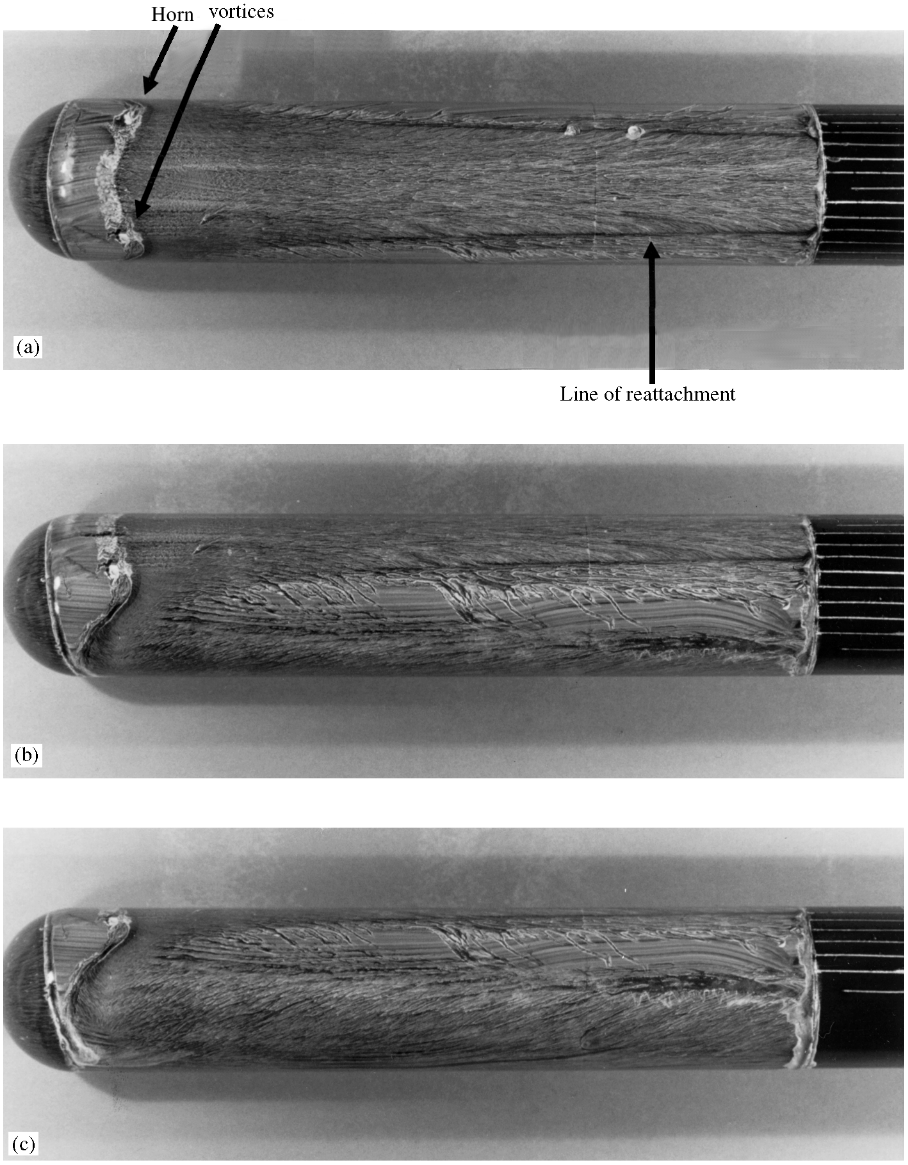

Figure 5. Surface flow visualizations at $\alpha = 10^\circ$ and $\mathrm{Re} = 27\,000$; (a) $\phi = 180^\circ$ (b) $\phi = 120^\circ$ and (c) $\phi = 90^\circ$.

Peake & Tobak (1982) data and their topology of skin friction lines which has been reproduced in Figure 2. The horn vortices are rooted in stable foci. The skin-friction patterns indicate a closed-type separation. The surface flow visualizations are usually inadequate to disclose the complex configuration of skin friction lines. Peake and Tobak in one of their later publications (Peak & Tobak 1982) propose patterns with a closed separation ring at the nose which incorporate horn vortices. A pair of reattachment lines is clearly evident over the full length of the afterbody at $\phi \simeq \pm 150^\circ$. The primary separation

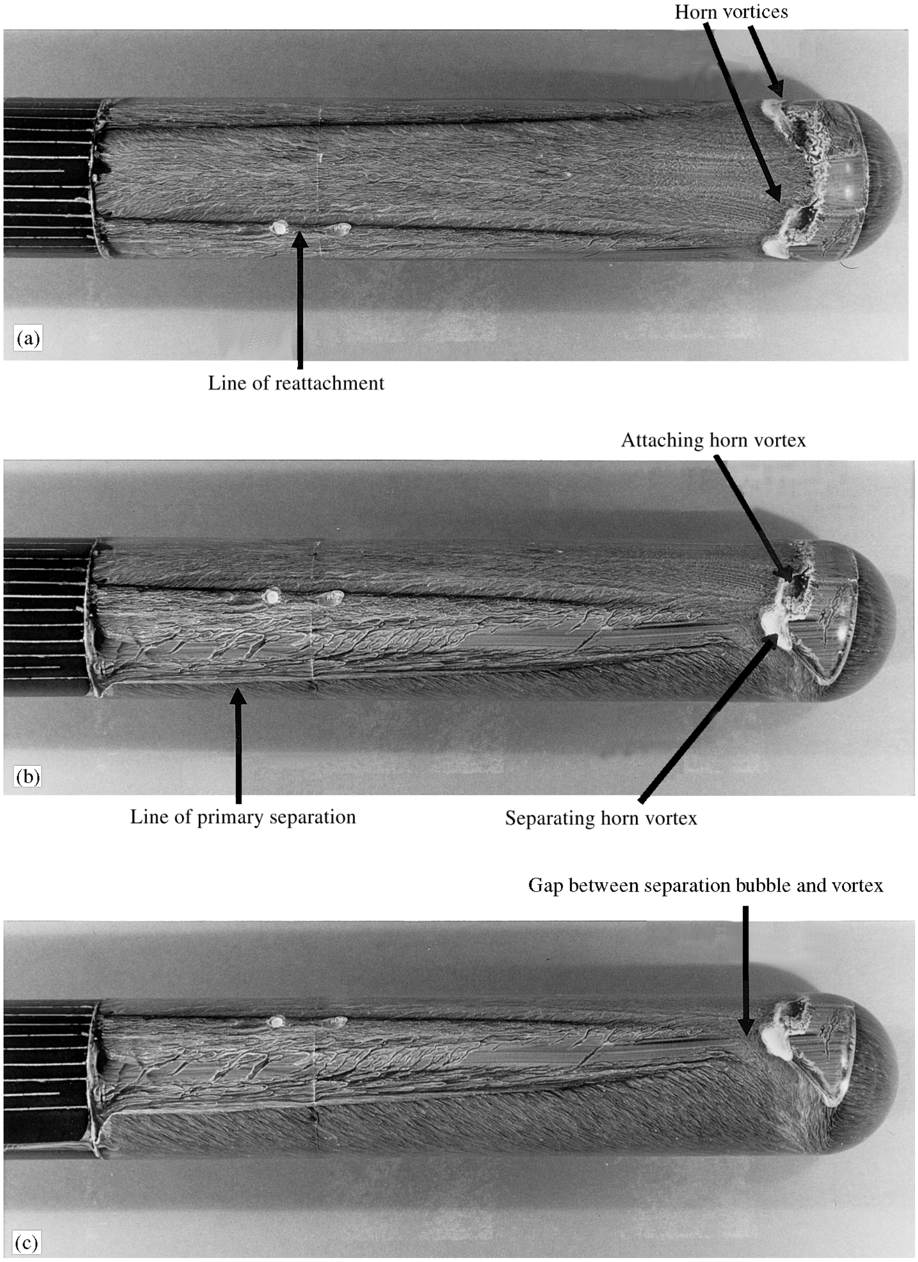

Figure 6. Surface flow visualization at $\alpha = 15^\circ$ and Re = 27 000; (a) $\phi = 180^\circ$ (b) $\phi = 120^\circ$ and (c) $\phi = 90^\circ$.

lines are not as pronounced, suggesting that the leeward vortices have not quite fully developed. These are local separation lines because they do not stem from saddle points. Pressure data presented in the next section confirm these observations.

At 15° angle of attack the separation bubble is confined to the leeward side of the model (Figure 6). Nose separation is closed, but further downstream we observe open separation.

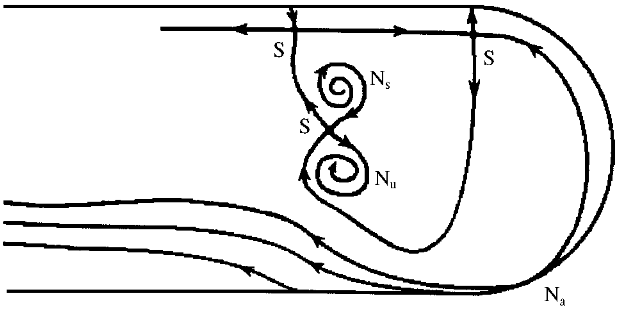

Figure 7. Possible skin fraction pattern consistent with the visualization of Figure 6(b). Unstable and stable modes mark the roots of horn vortices.

Fluid originating upstream can reach both sides of the leeward separation lines along the afterbody. Two primary separation lines stretch along the afterbody from $x/R = 3{\cdot}0$, $\phi = \pm 100°$ to the trailing edge of the model ($\phi = \pm 80°$). Pairs of reattachment lines are also visible from $x/R = 3{\cdot}6$, $\phi = \pm 130°$ to the trailing edge ($\phi = \pm 150°$). Lines of secondary separation are also apparent. Vortex sheets emanating from the primary and secondary separation lines merge into a single sheet and roll up to form two axial vortices (Costis *et al.* 1989). There is very little fluid motion in the area between the lines of separation and reattachment. The separation bubble on the nose and the axial leeward vortices are still apart [see Figure 6(c)]. Their interaction is expected to be minimal. Notice that there is a well defined gap of what appears to be attached flow that separates the nose bubble from the leeward vortices.

Some authors object to the use of the term "bubble" for nose separation, if the lines of separation do not form rings, as is the case for zero incidence. Indeed, the term is used very restrictively by investigators of three-dimensional flow separation. However, in airfoil aerodynamics, leading-edge separation and reattachment which usually occur at low Reynolds numbers is often referred to as a "separation bubble". The velocity profiles across such bubbles are inflectional and therefore very unstable. For slightly higher Reynolds numbers, the flow goes turbulent soon after separation. This is a very significant feature of the flow in the present case, because it implies that the flow on the windward side of the model will turn turbulent very near the nose. This is a drastic departure from flows over bodies that have no separation bubble near their noise. Such is the case with a prolate spheroid on which it is possible that for many body diameters downstream, the flow could be laminar on the windward side of cross-flow separation but turbulent on the leeward side (Kreplin *et al.* 1982, Costis & Telionis 1983; Costis *et al.* 1989).

For $\alpha = 15°$, the horn vortices are located around $\phi = \pm 130°$, $x/R = 2{\cdot}3$, but the flow visualization of Figure 6 displays a significant new pattern. The familiar pair of the roots of the horn vortices appear as light patches. This is where the visualization dye accumulates. But in the neighbourhood of the light patches there are also two very dark regions. We interpret this as evidence of the existence of another pair of vortices normal to the surface of the model. Because the dye is totally removed there, these horn vortices must be vortices of attachment. The one pair must be rooted along stable foci and the other along unstable foci; a pattern that has not been observed before. The first represents a separating horn and the other an attaching horn. A possible pattern of the topology of skin friction lines consistent

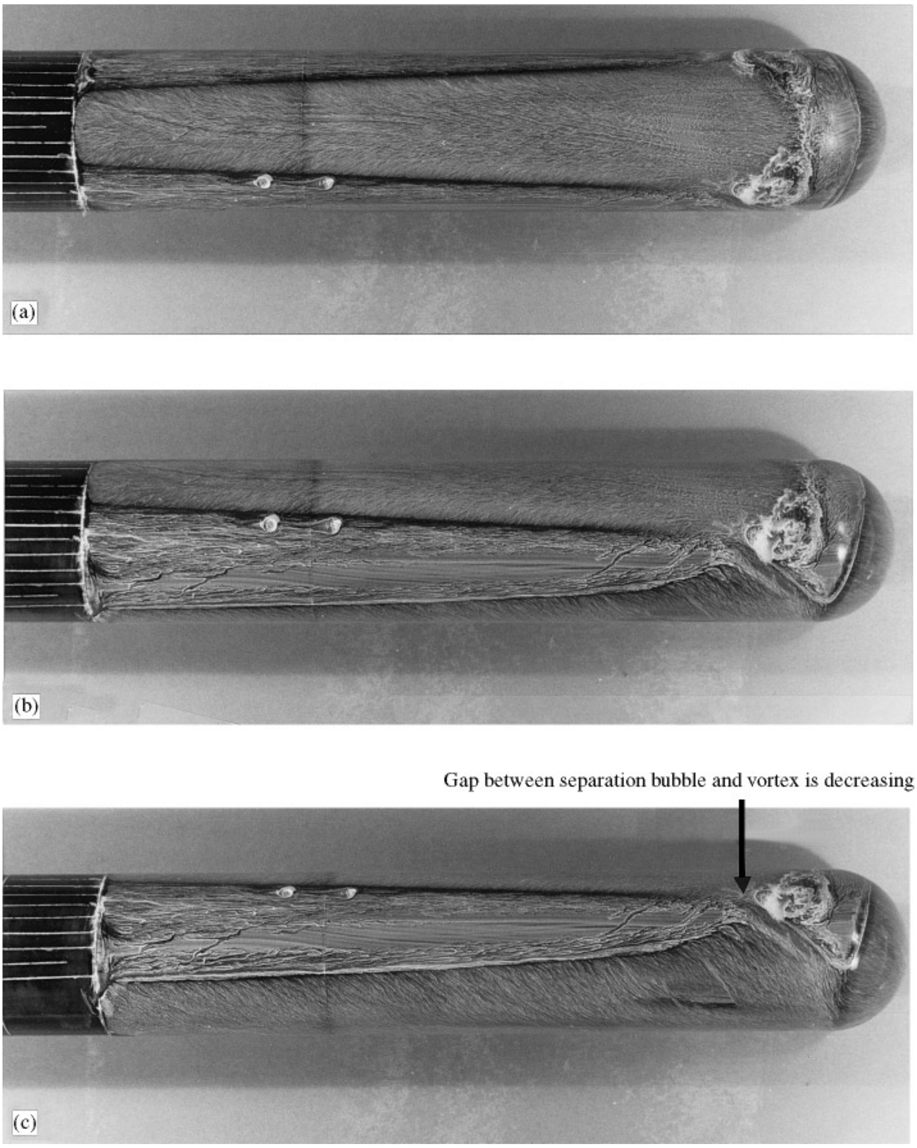

Figure 8. Surface flow visualizations at $\alpha = 20^\circ$ and Re = 27 000; (a) $\phi = 180^\circ$ (b) $\phi = 120^\circ$ and (c) $\phi = 90^\circ$.

with the experimental evidence as well as with the topological law constraining the number of saddle and nodal points (Tobak & Peake 1982) is presented in Figure 7. This represents the view from $\phi = 120^\circ$ and is consistent with Figure 6(b). Note that the stable focus, N_s, and the unstable focus N_u, stem from two neighbouring branches of a saddle point. This nose bubble can represent closed separation in the strictest sense adopted by Hsieh & Wang (1996) and Hsieh (1997) because the separating horn vortex may be simply reattaching at the stable focus, thus forming a “handle.” Fluid being removed along N_u could actually be

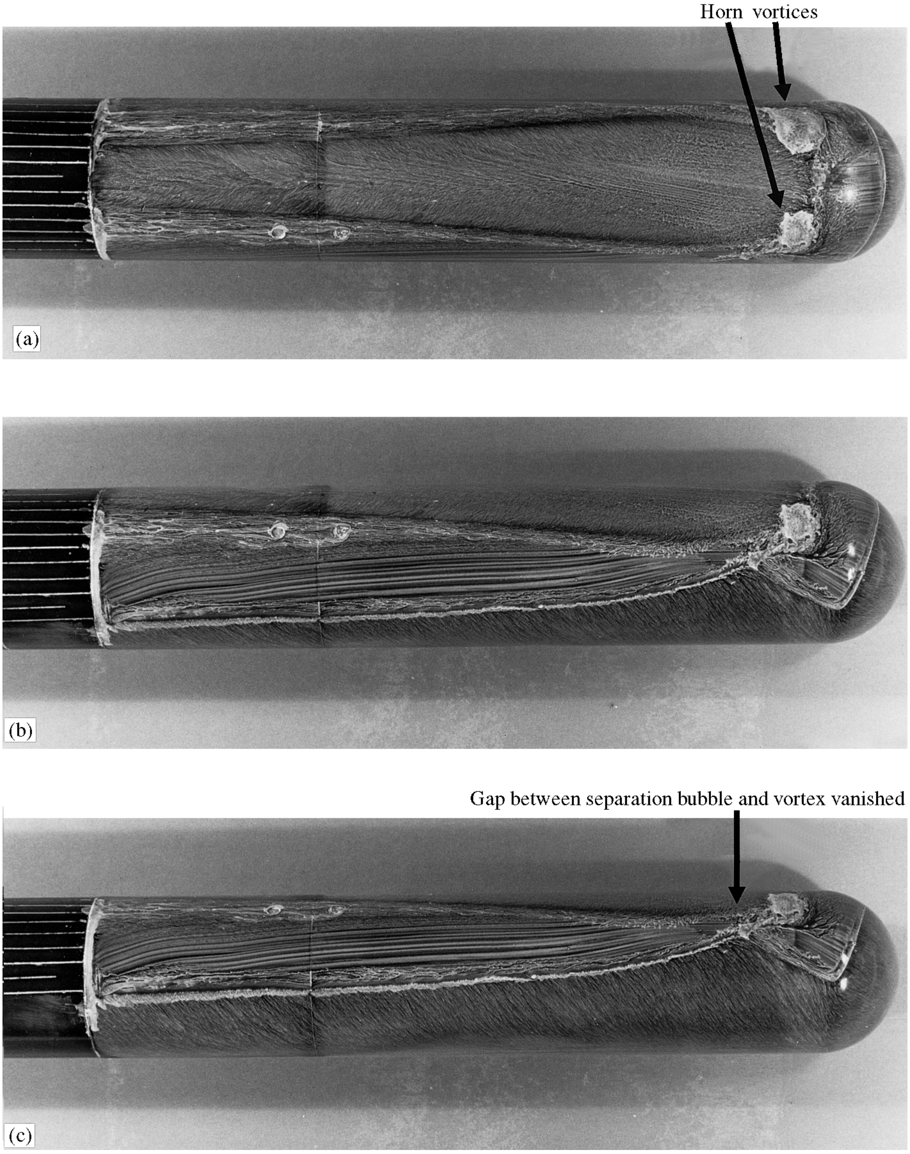

Figure 9. Surface flow visualizations at $\alpha = 25^\circ$ and Re = 27 000; (a) $\phi = 180^\circ$ (b) $\phi = 120^\circ$ and (c) $\phi = 90^\circ$.

returned to the bubble at N_s and thus no communication with the stream that comes from upstream is necessary.

At $\alpha = 20^\circ$, the separation bubble becomes smaller both axially and circumferentially and stretches over only the top half of the hemispherical cap. The horn vortices create large patterns of swirling imprints near the nose of the model (Figure 8). An obvious difference from the previous figures is the heavy amount of titanium dioxide collected around the roots of the horn vortices. Again, light and dark spots indicate the possibility of separating

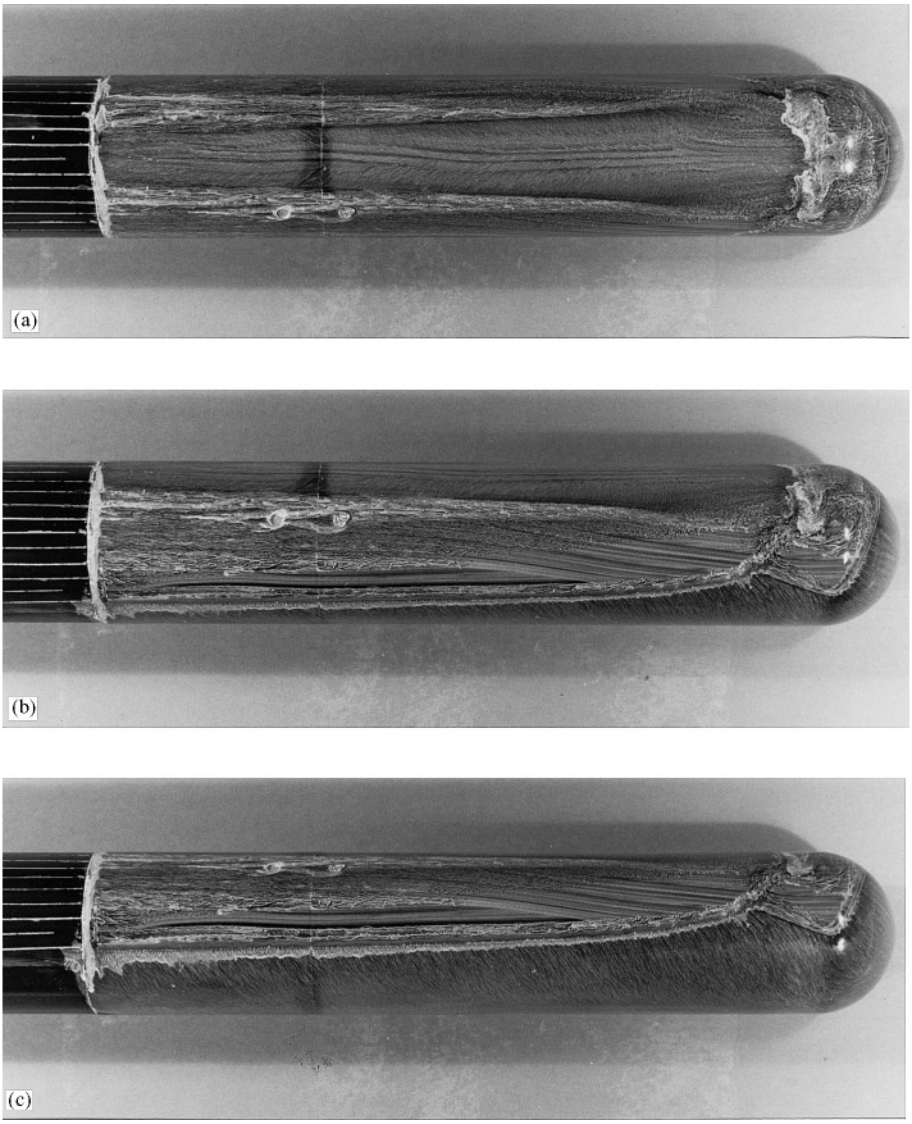

Figure 10. Surface flow visualizations at $\alpha = 30^\circ$ and Re = 27 000; (a) $\phi = 180^\circ$ (b) $\phi = 120^\circ$ and (c) $\phi = 90^\circ$.

and attaching horn vortices. The swirling motions of the horn vortices eliminate the paintbrush marks within part of the separation bubble. Narrow gaps separate the horn vortices and the leeward vortices from each other; hence, the flow retains its open separation character. Lines of separation and reattachment remain nearly at the same position as in the 15°-incidence case. The origins of the leeward vortices are located near $x/R = 3{\cdot}70$. From the leeward view, $\phi = 180^\circ$, we observe that the skin friction patterns do not display any features of vortex asymmetry.

At 25° angle of attack, the separation bubble and the leeward vortices merge together to form a single separation region (Figure 9). The lines of primary and secondary separation

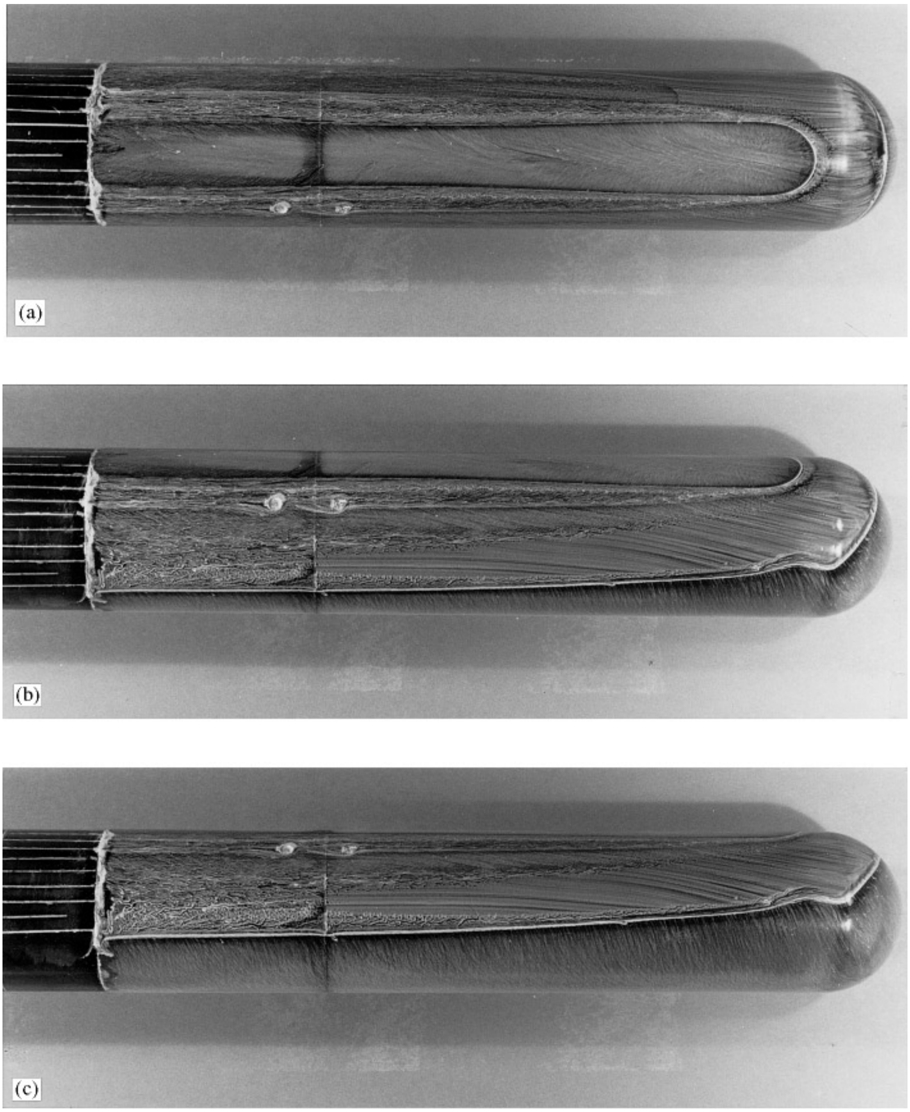

Figure 11. Surface flow visualizations at $\alpha = 45^\circ$ and Re = 27 000; (a) $\phi = 180^\circ$ (b) $\phi = 120^\circ$ and (c) $\phi = 90^\circ$.

connect with the separation and reattachment lines of separation bubble, respectively. The horn vortices of detachment can still be clearly detected on the suction side of the hemispherical cap but there is no evidence of attaching horn vortices.

At $\alpha = 30^\circ$, the photographs show some weak swirling motions near the nose (Figure 10). A kink appears on the primary separation line where the separation bubble and the leeward vortices merge. The trace of the horn vortices completely disappear at angles of attack $\alpha = 35^\circ$, 40° and 45°. Due to lack of space, only the last case is displayed here in Figure 11. The leeward vortices produce a pattern known as "necklace vortex" or "horseshoe vortex" (Yates & Chapman 1991; Hsieh & Wang 1995). There is no asymmetry detected.

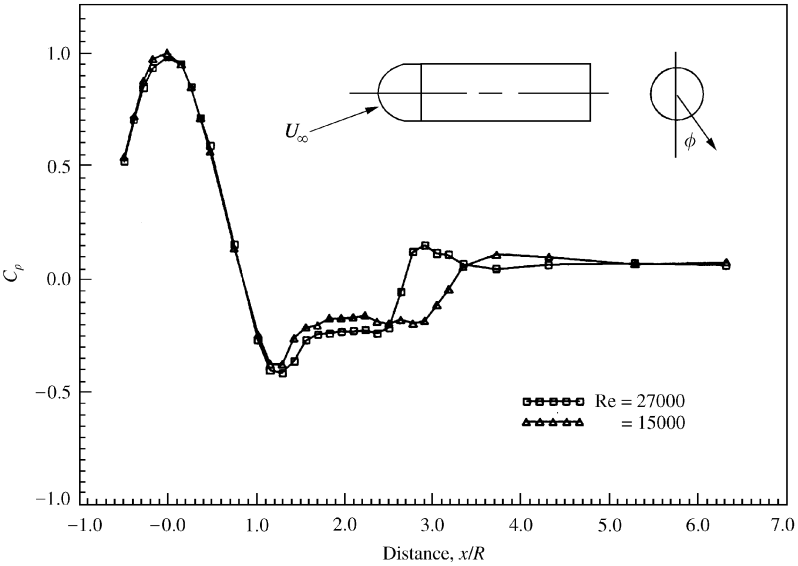

Figure 12. Axial pressure distributions on a hemisphere-cylinder at $\alpha = 0°$ and two different Reynolds numbers.

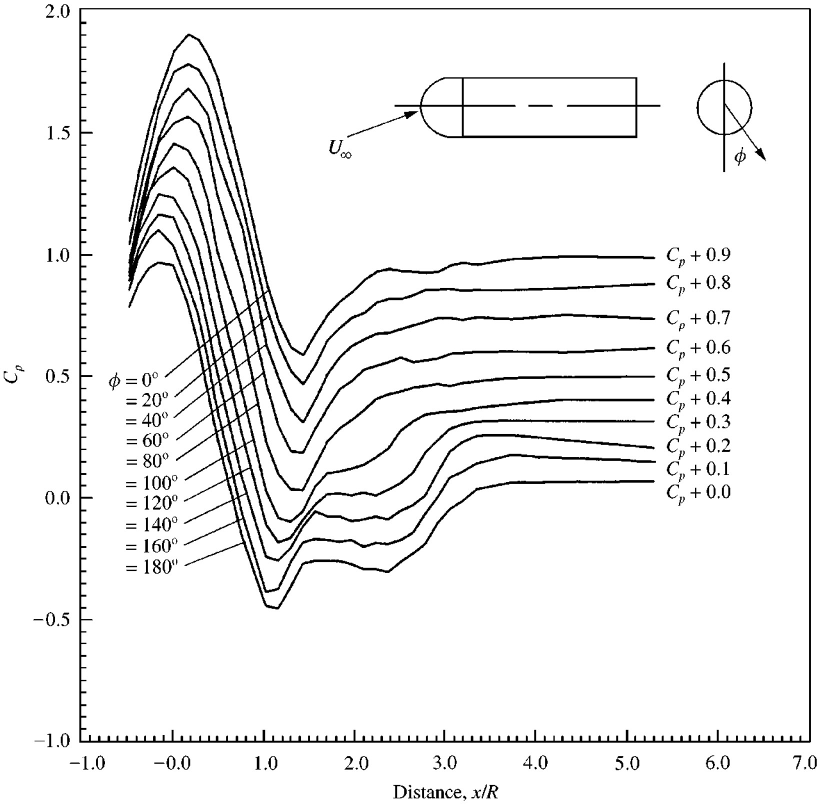

Figure 13. Axial pressure distributions on a hemisphere-cylinder at $\alpha = 10°$ and Re = 15 000 with added constants.

3.2. PRESSURE MEASUREMENTS

Static pressure distributions on the test-section wall of the ESM Wind Tunnel were collected first to document the level of wall interference. A row of eighteen 1/16 in (1.59 mm) diameter orifices, 1 in (25.4 mm) apart, were placed on the top wall of the test section along the plane of symmetry (Figure 4). The experiment was carried out at a Reynolds number of $2{\cdot}7 \times 10^4$ for four different cases: (i) no model in the test section and the model placed in the test section at (ii) 10°, (iii) 20° and (iv) 30° angles of attack. The interference between the walls and the model was plotted and presented in Hoang (1991). Even in the worst case, when the model was at $\alpha = 30°$, the largest deviation of the wall pressure coefficients from the no-model case is 0·014. To test the accuracy and repeatability of the measurements, pressure data on the model were obtained at a Reynolds number of $2{\cdot}7 \times 10^4$ in two different facilities, the ESM Wind Tunnel and the VPI Stability Wind Tunnel. The ESM Wind Tunnel has a free-stream turbulence level of 0·5%, compared to 0·018% of the VPI Stability Wind Tunnel. The blockage ratios, i.e. model frontal area to tunnel cross-sectional area, were 0·008 and 0·0006 for the ESM Wind Tunnel and the VPI Stability Tunnel, respectively. Results are presented in Hoang (1991). The flow quality of the wind tunnels such as level of free-stream turbulence and blockage ratio seem to have a non-negligible effect on the value of the local pressure coefficients but not the overall behaviour of the flow. The flow still retains its basic characteristics. With such small blockage values, it is believed that the deviation between the two cases are due to tunnel turbulence level.

At zero-degree incidence, all pressure data were taken at $\phi = 180°$ along the x-axis. Pressure coefficients at $\phi = 0°$, 90° and 270° were used for aligning the model with the tunnel. Figure 12 displays axial pressure distributions at $\alpha = 0°$ for two different Reynolds numbers, $\text{Re} = 1{\cdot}5 \times 10^4$ and $2{\cdot}7 \times 10^4$. The flow stagnates at $x/R = 0$ where the highest pressure coefficient, $C_p = 1{\cdot}0$, is registered. The pressure coefficient progressively decreases to a minimal value of $-0{\cdot}38$ for Reynolds number of $1{\cdot}5 \times 10^4$ and drops slightly lower, to $-0{\cdot}41$, for $\text{Re} = 2{\cdot}7 \times 10^4$ at $x/R = 1{\cdot}3$. The flow then attempts to recover, but separates approximately at $x/R = 1{\cdot}5$. Within the separated region (or the separation bubble), pressure coefficients stay nearly constant at about $-0{\cdot}25$. For $\text{Re} = 1{\cdot}5 \times 10^4$, the flow reattaches at $x/R = 3{\cdot}0$, as indicated by a sudden jump in pressure coefficients. After the point of reattachment, the pressure coefficients level off to zero along the afterbody of the model. At a higher Reynolds number, $\text{Re} = 2{\cdot}7 \times 10^4$, the point of reattachment is at about $x/R = 2{\cdot}4$, implying that the separation bubble decreases in size with increasing Reynolds number. Pressure coefficients along the afterbody also remain at zero.

Figure 13 displays axial surface pressure distributions for $\alpha = 10°$ and a Reynolds number of $1{\cdot}5 \times 10^4$. Although data were measured from $\phi = 0°$ to 180° in 10° increments, for the purpose of clarity, only results at every 20° were plotted. Nevertheless, the curves were not easily distinguishable if plotted along the same coordinate axes. A constant value of 0·1 was added to each curve to separate them from each other. As in the zero-incidence case, the distribution displays a flat region of constant pressure coefficients in the range of $1{\cdot}3 \leqslant x/R \leqslant 2{\cdot}5$, $\phi = 180°$ confirming the presence of a separation bubble. The flat region disappears for $\phi < 100°$, although the bubble still exists, as shown in the flow visualization photographs. Apparently, the separation bubble in the area between $0° \leqslant \phi \leqslant 100°$ is too small to cause any disturbance in the pressure distribution. The equivalent pressure coefficient contours are displayed in Figure 14. In this figure all the obtained data were employed to construct the contours. Here the distance l is measured along the model axis of revolution and $l = 0$ is at the tip of the model (see Figure 3). Large pressure gradients are shown in the nose region ahead of the separation bubble. Along the afterbody of the model, pressure coefficients remain somewhat uniform. If plotted along the circumferential (Hoang 1991) the pressure distributions display characteristics similar to the potential flow over a two-dimensional circular cylinder placed normal to the flow, especially at locations far downstream of the nose. The pressure is close to stagnation values both fore and aft and decreases on the flanks of the model. The data at $\alpha = 10^\circ$ and $\mathrm{Re} = 2{\cdot}7 \times 10^4$ (Hoang 1991) indicate that the separation bubble decreases somewhat in size, which is consistent with the zero-degree-incidence case. Pressure coefficient contours show a large region of low pressure in the vicinity of the separation bubble, $x/R = 1{\cdot}0$ to $2{\cdot}0$.

Axial pressure distributions at 20° incidence and a Reynolds number of $1{\cdot}5 \times 10^4$ are shown in Figure 15. The separation bubble is now confined to the top of the hemispherical cap and appears as a region of nearly constant pressure coefficients. It has increased in length when compared with the 10° incidence case for the same Reynolds number.The pressure plots reveal a peculiar behaviour; the curves become jagged within the separation bubble, especially at $\phi = 180^\circ$. During the experiment, the sampling time was doubled, from three seconds per data point to six seconds, to eliminate flow unsteadiness from the measurements. However, the same characteristic persists. This behaviour may be associated with the presence of the roots of horn vortices. Pressure coefficient contours are shown in Figure 16.

Figure 17 presents axial pressure distribution plots of a hemisphere-cylinder at $\alpha = 20^\circ$ but at a higher Reynolds number, $\mathrm{Re} = 2{\cdot}7 \times 10^4$. The jagged characteristic, displayed by the pressure curves at the lower Reynolds number has vanished. But unlike the previous cases, pressure coefficients within the separation bubble do not remain constant. As the curves cross the separation bubble, the pressure coefficient progressively drops to a minimum before leaving the separated region. Since the separation bubble is located between two horn vortices with opposite rotational directions, it is possible that the strong swirling motions of horn vortices induce a velocity component within the separation bubble. This activity energizes the separated region and appears as a nonflat domain in the pressure distribution.

For $\alpha = 30^\circ$ and $\mathrm{Re} = 1{\cdot}5 \times 10^4$, the pressure contours are displayed in Figure 18. At this incidence, the separation bubble and the leeward vortices have already merged into one large region of separation (Figure 10). Pressure contours between $100^\circ \leqslant \phi \leqslant 160^\circ$ and beyond $L/R = 1$ reside entirely inside the separated region; consequently, pressure coefficients remain constant along the afterbody of the model. Although the leeward vortices originate at $x/R = 1{\cdot}2$, the swirling motion does not begin until $x/R = 2{\cdot}64$ and $\phi = 160^\circ$. Plots of the circumferential distribution of pressure are shown in Figure 19. At stations near the nose, the pressure is very low on the leeward side. Further away from the nose, at $x/R = 2{\cdot}78$ a weak dip emerges, indicating the presence of an active leeward vortex. Quite often this is referred to in literature as the “footprint” of the vortex. The location of the vortex core remains unchanged along the afterbody of the model at $\phi = 160^\circ$. Very deep dips in the circumferential pressure curves demonstrate the existence of strong leeward vortices. The dips are most pronounced between $x/R = 3{\cdot}05$ to $5{\cdot}29$ and then gradually become shallower toward $x/R = 6{\cdot}32$. This suggests that the leeward vortices are either lifting off from the surface of the model or lose vorticity due to some sort of vortex breakdown. For a higher Reynolds number, $\mathrm{Re} = 2{\cdot}7 \times 10^4$, similar characteristics are displayed as shown in Figure 20. The vortex cores are now approximately located at $\phi = 150^\circ$, along the afterbody of the model. This indicates that the leeward vortices move away from each other at higher Reynolds number.

A complete set of pressure contours and circumferential pressure distributions for the two Reynolds numbers tested may be found in Hoang (1991).

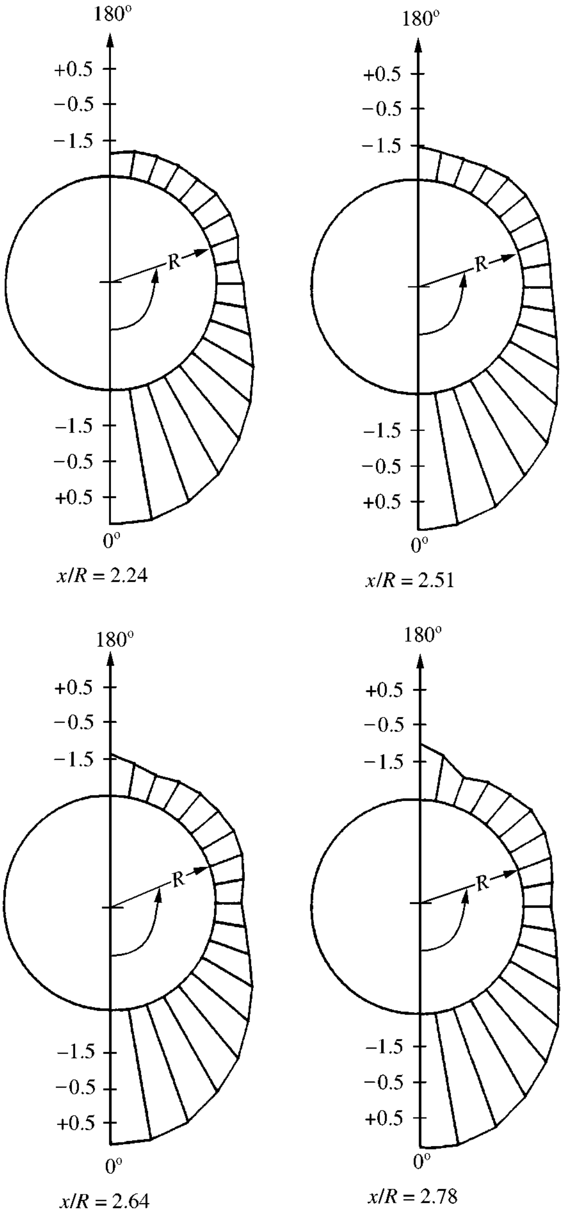

$x/R = 2.24$ $x/R = 2.51$

$x/R = 2.64$ $x/R = 2.78$

Figure 19. Circumferential pressure distributions on a hemisphere-cylinder at $\alpha = 30°$ and Re = 15 000.

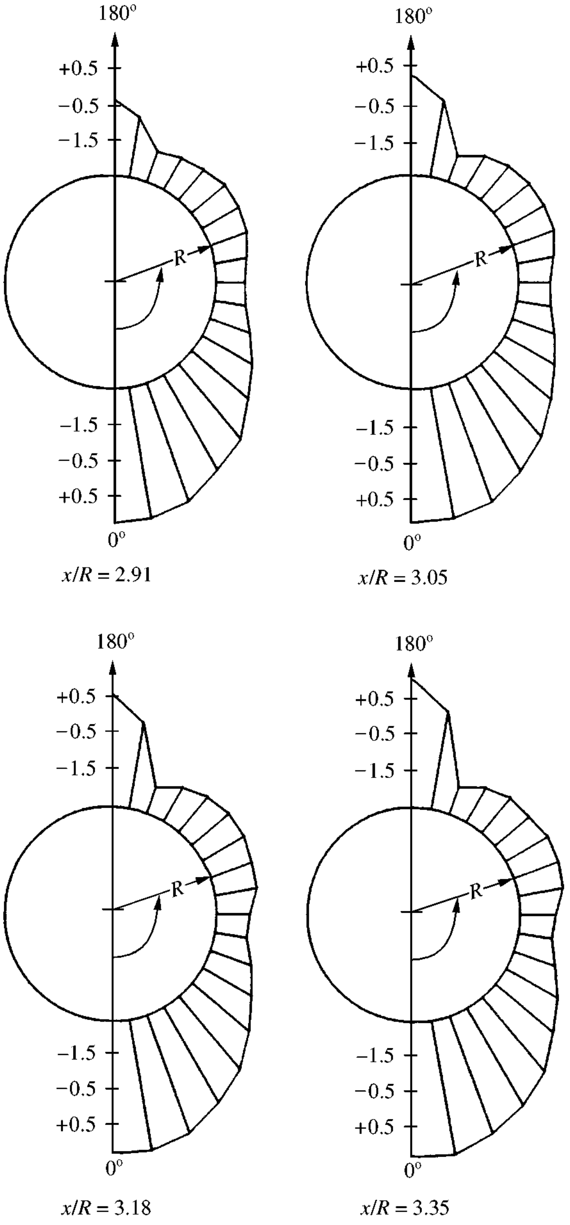

x/R = 2.91

x/R = 3.05

x/R = 3.18

x/R = 3.35

Figure 19. Continued

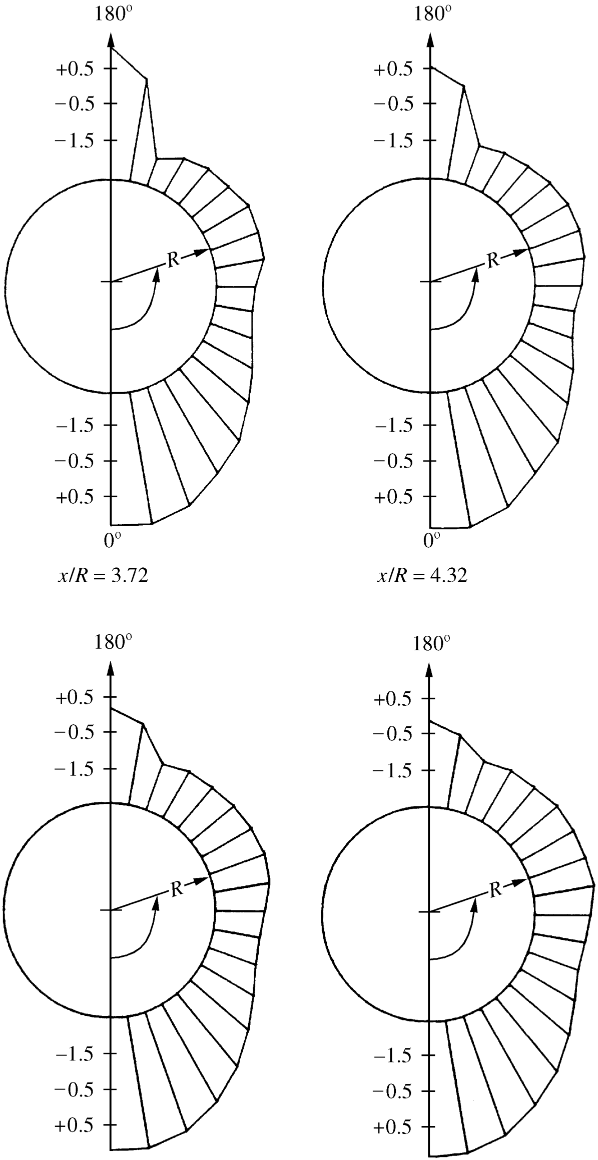

$x/R = 3.72$ $x/R = 4.32$

$x/R = 5.29$ $x/R = 6.32$

Figure 19. Continued

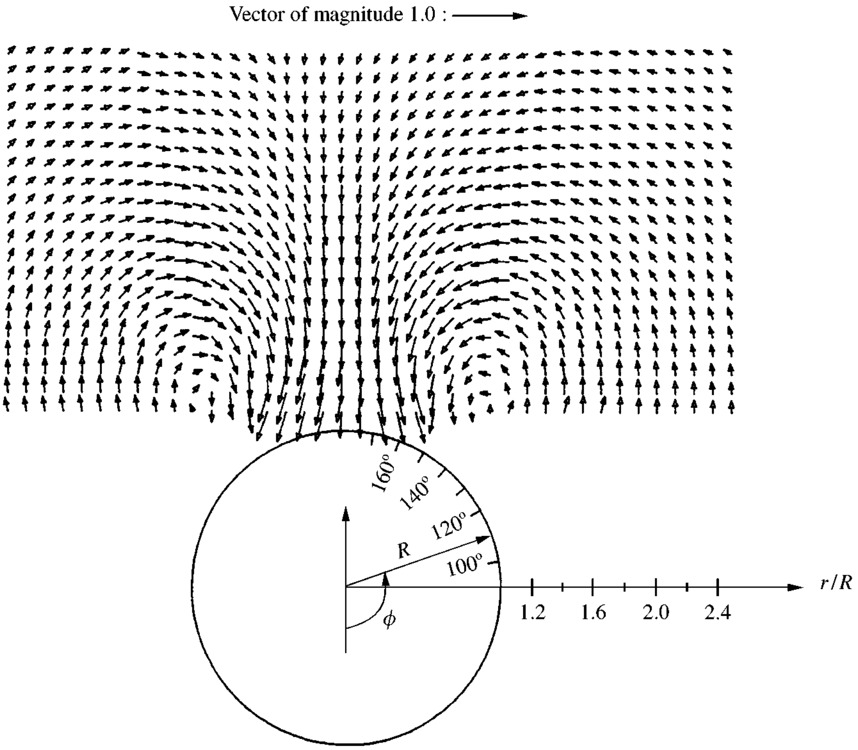

Figure 21. Velocity field at $\alpha = 20^\circ$ and Re = 27 000 with no bead.

3.3. Velocity Measurements

Wake velocity measurements of the hemisphere-cylinder presented in this section were obtained in a plane perpendicular to the free-stream velocity at a Reynolds number of $2{\cdot}7 \times 10^4$ and $x/R = 20{\cdot}5$. The cross-flow velocity vectors on this plane for the hemisphere-cylinder at $\alpha = 20^\circ$ and 30° are displayed in Figure 21 and 22, respectively. The circle displayed in these figures represents the projection of the tail of the model on the plane of measurement and is included here only as a visual aid. A pair of symmetrical leeward vortices can be seen in these figures. The cores of these vortices are closer to the surface of the model for the 20° than for the 30° incidence case, but the flowfield is symmetric in both cases. The symmetric pattern of the leeward vortices displayed by both velocity measurements and flow visualization results justified taking pressures only on half of the model.

Axial velocity components are also available for all the data presented in this section. A typical example of axial velocity contours is presented in Figure 23. The velocity is reduced in terms of the free-stream velocity. A region of velocity defect appearing in the measuring domain is probably due to the model's blockage. A surprising fact is that there is no increase of axial velocity in the core of the leeward vortices. In contrast to the present findings, the axial velocity components in the core of the vortices of a delta wing can reach values as high as three times the free-stream velocity (Redinoitis *et al.* 1991). There is also some asymmetry displayed but this may be due to experimental error because no evidence of asymmetry can be found in the circumferential velocity.

Measurements shown in the rest of this section were obtained at a Reynolds number of $2{\cdot}7 \times 10^4$ and $\alpha = 30^\circ$ to investigate vortex field asymmetries induced by the placement of

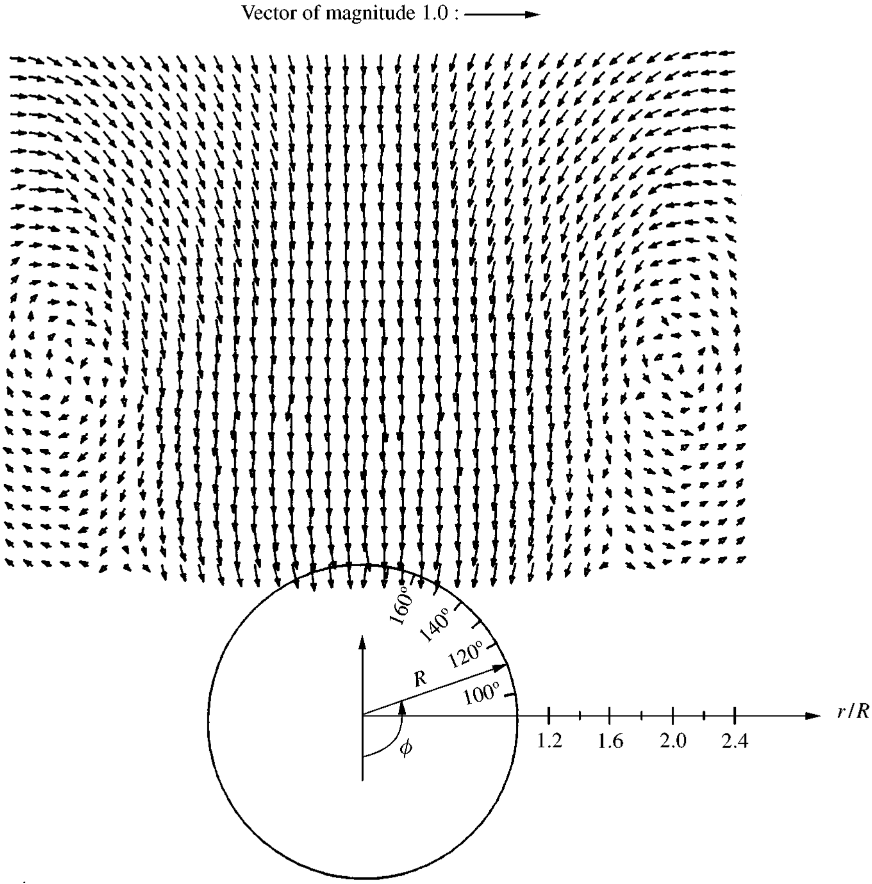

Figure 22. Velocity field at $\alpha = 30°$ and Re = 27 000 with no bead.

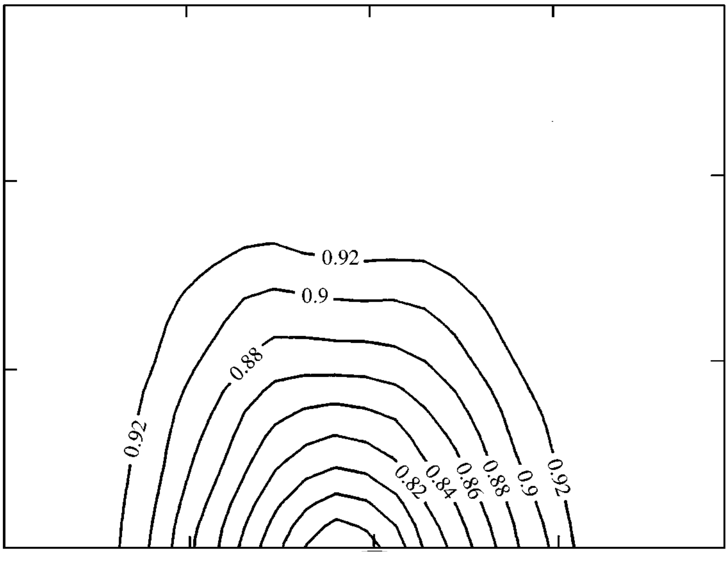

Figure 23. Axial velocity component contours at $\alpha = 30°$ and Re = 27 000 with no bead.

physical disturbances in the neighbourhood of the separation bubble. Two different sizes of beads were employed at various positions. The first one, bead #1 was a 1/16 in (1·59 mm) diameter hemisphere with a height of 1/32 in (0·79 mm). The second, bead #2 was a 1/32 in (0·79 mm) by 1/24 in (1·06 mm) rectangle with a height of 1/64 in (0·40 mm). When bead #1 was mounted on the hemisphere-cylinder at $x/R = 0{\cdot}5$ and $\phi = 30°$, i.e. in front of the separation bubble that develops on the nose of the model, the flowfield exhibited a very low degree of vortex asymmetry (not shown here due to lack of space). The effect of the bead on the overall flow behaviour was minimal.

The bead was then mounted at different azimuthal locations but always at $x/R = 0{\cdot}5$, i.e. a little ahead of the bubble. With bead #1 mounted at $\phi = 70°$, the flow pattern became highly asymmetric. The right leeward vortex (the side with the bead) dominated the wake and spread itself over a much larger region than the left leeward vortex. As expected, the locations of the vortices changed. The dominant vortex moved toward the surface of the model while the other moved further away. The ratio of the maximum vorticity between the right and left vortex was 3·2 to 1·0.

With the bead #1 mounted at $x/R = 0{\cdot}5$ and $\phi = 90°$, the asymmetric pattern is even more pronounced than in the previous case. Both vortices gain considerable amount of strength and size. At the core of the right vortex, vorticity increases from 3·2 to 6·0; similarly, the left vortex has an increase in strength from $-1{\cdot}0$ to $-3{\cdot}0$. Velocity field and vorticity contours, when bead #1 was placed at $x/R = 0{\cdot}5$ and $\phi = 120°$, are shown in Figure 24. The flowfield pattern displays the highest degree of asymmetry. Both leeward vortices reach their maximum strength, however, with a slight decrease in size. The distance between the vortices is the largest recorded in these experiments. Only half of the left vortex is contained within the measuring domain. The axial velocity component for this case once again shows no evidence of the violent vortical motion and minimal indications of asymmetry (Figure 25). When bead #1 was positioned at $x/R = 0{\cdot}5$ and $\phi = 150°$, the degree of asymmetry decreased somewhat.

Bead #1 was then moved to a location inside the separation bubble at $x/R = 1{\cdot}8$ and $\phi = 120°$. For this case, Figure 26 displays a lesser degree of asymmetry than the flowfield pattern when bead #1 was placed in front of the separation bubble and at the same azimuthal location. Bead #1 was then mounted behind the separation bubble at $x/R = 2{\cdot}5$ and $\phi = 120°$. The flowfield then assumed an almost symmetric configuration. The asymmetric pattern switched side when bead #1 was placed at $x/R = 0{\cdot}5$ and $\phi = 280°$. Velocity fields were measured with a smaller bead (bead #2) positioned at $x/R = 0{\cdot}5$ and $\phi = 120°$. A somewhat lesser degree of asymmetry than when a larger bead was placed at the same position was then observed.

4. CONCLUSIONS

The flow over a hemisphere-cylinder at low Reynolds numbers develops a separation bubble near the juncture of the hemisphere with the cylinder at all incidences. The evidence presented here indicates that this bubble represents closed separation. At low incidences, it forms a ring around the nose, while at high incidences it is confined to the leeward side of the body. A basic feature of the separation bubble is the horn vortices which are rooted within the separated region. These structures appear to influence the development of leeward vortices which evolve in the form of open separation, even though the latter originate downstream of the separation bubble. As the incidence increases, the two patterns merge into each other to form a horseshoe vortex. The development of asymmetries in the wake is strongly influenced by disturbances placed in the neighbourhood of the separation bubble. In fact, it appears that the most effective location of the disturbance to generate the most violent asymmetry is the root of the horn vortices.

Our flow visualizations contain evidence of unstable foci of the skin friction topology. This implies that, at such foci, attaching horn vortices may be rooted. Attaching and detaching vortices are rooted very close to each other. It is therefore very possible that they are connected immediately above the body, essentially forming a "handle." Such a behaviour must be encouraged by the natural tendency of vortices to reconnect.

The evidence presented here indicates that events in the neighbourhood of the model nose strongly influence the separation characteristics for many diameters downstream. It is therefore important in numerical calculations to employ a tight grid in this region in order to predict accurately the flow there. Moreover, designers of engineering components should keep in mind that small physical disturbances in the nose region could have great effect on the separation characteristics over the entire body. This was most clearly demonstrated by placing a small bead on the nose of the body.

The experiments discussed in this paper have been conducted in the range of Reynolds numbers for which the flow is always laminar. Earlier studies in our facilitates have indicated that at these Reynolds numbers, even tripping of the boundary layer does not affect the laminar character of the flow. We observed that small changes of the Reynolds number do not lead to drastic changes of the flow field. However, some small modifications of the flow properties, especially in the immediate neighbourhood of the bubble, were observed.

Separation bubbles are common in low-Reynolds number flows. Studies at such Reynolds numbers are quite significant because flow through bubbles is very unstable. The presence of bubbles at low Reynolds numbers is a strong indication that, for flow over the same configuration at higher Reynolds numbers, transition may develop in the same neighbourhood. Indeed, in the present case, we anticipate that since the bubble is confined to the leeside of the body, at higher Reynolds numbers, the flow downstream of the bubble may quickly turn turbulent, whereas the flow on the windward side could be sustained laminar. In fact, this is in agreement with the findings of Kreplin *et al.* (1982), who documented much higher shearing stresses on the leeside of the line of separation than on the windward side.

ACKNOWLEDGMENT

This work was supported by the NASA-Langley Research Center Experimental Methods Branch and the Theoretical Aerodynamics Branch (Grant Numbers NGT-50144 and NAS1-18471). The models used were also supplied by NASA. Special thanks are due to M. Salas, W. L. Sellers and Dr G. S. Jones. The authors are indebted to Dr T. Hsieh of Naval Surface Warfare Center for his constructive criticism and valuable suggestions.

REFERENCES

BARBER, K. M. & SIMPSON, R. L. 1991 Mean velocity and turbulence measurements of flow around a 6:1 prolate spheroid. AIAA Paper 91-0255.

CHESNAKAS, C. J. & SIMPSON, R. L. 1994 Full three-dimensional measurements of the cross-flow separation region of a 6:1 prolate spheroid. *Experiments in Fluids* **17,** 68–74.

COSTIS, C.E., HOANG, N.T. & TELIONIS, D. P. 1989 Laminar separating flow over a prolate spheroid. *Journal of Aircraft* **26,** 810–816.

COSTIS, C. & TELIONIS, D. P. 1983 Unsteady vortical wakes over a prolate spheroid. *AIAA Journal* **20,** 1189–1193.

DEGANI, D. & TOBAK, M. 1991 Numerical experimental and theoretical study of convective instability of flows over pointed bodies at incidence. AIAA Paper 91-0291.

DEGANI, D. 1991 Effect of geometrical disturbance of vortex asymmetry. *AIAA Journal* **29,** 560–566.

Ericsson, L. E. & Redding, J. P. 1986 Asymmetric vortex shedding from bodies of revolution. *Progress in Astronautics and Aeronautics Series* **19,** 243–296.

Han, T. Y. & Patel, V. C. 1979 Flow separation on a spheroid at incidence. *Journal of Fluid Mechanics* **92,** 643–657.

Hoang, N. T. 1991 The hemisphere-cylinder at an angle of attack. VPI & SU, Ph.D. Dissertation, Blacksburg, VA, U.S.A.

Hoang, N. T. Telionis, D. P. & Jones, G. S. 1990 The hemisphere-cylinder at an angle of attack. AIAA Paper 90-0050.

Hoang, N. T., Rediniotis, O. K. & Telionis, D. P. 1991 Separation over axisymmetric bodies at large angles of attack. AIAA Paper 91-0277.

Hsieh, T. 1975a Low supersonic, three-dimensional flow about a hemisphere-cylinder. AIAA Paper 75-836.

Hsieh, T. 1975b Hemisphere-cylinder in low supersonic flow. *AIAA Journal 13*, 1551–1552.

Hsieh, T. 1977a An investigation of separated flow about a hemisphere-cylinder at incidence in the Mach number range from 0.6 to 1.5. AIAA Paper 77-179.

Hsieh, T. 1977b Analysis of velocity measurements about a hemisphere-cylinder using a laser velocimeter. *Journal of Spacecraft and Rockets* **14,** 280–283.

Hsieh, T. 1977c Low supersonic flow over hemisphere-cylinder at incidence. *Journal of Spacecraft and Rockets* **14,** 662–668.

Hsieh, T. & Wang, K. C. 1976 Concentrated vortex on the nose of an inclined body of revolution. *AIAA Journal* **14,** 698–700.

Hsieh, T. & Wang, K. C. 1996 Three-dimensional separated flow structure over a hemisphere-cylinder. *Journal of Fluid Mechanics* **324,** 83–108.

Keener, E. R. & Chapman, G. T. 1977 Similarity in vortex asymmetries over slender bodies and wings. *AIAA Journal* **15,** 1370–1372.

Kreplin, H. P., Vollmers, H. & Meier, H. U. 1982 Measurements of the wall shear stress on an inclined prolate spheroid. *Z. Flugwiss Weltraumforschung* **6,** 248–252.

Maskell, E. C. 1955 Flow separation in three-dimensions. Royal Aircraft Establishment, Report No. Aero 2565.

Meade, A. J., & Schiff, L. B. 1987 "Experimental study of three-dimensional separated flow surrounding a hemisphere-cylinder at incidence," AIAA Paper No. 87-2492.

Meier, H. U. & Kreplin, H. P. 1980 Experimental investigations of boundary layer transition and separation on a body of revolution. *Z. Flugwiss Weltraumforschung* **4,** 65–71.

Moskovitz, C. A., Hall, R. M., and Dejarnette, F. R. 1989 Effects of nose bluntness roughness and surface perturbations on the asymmetric flow past slender bodies at large angles of attack. AIAA Paper 89-2236.

Patel, V. C. & Baek, J. H. 1983 Calculation of boundary layers and separation on a spheroid at incident. Presented at Numerical and Physical Aspects of Aerodynamic Flows Conference, Long Beach, CA.

Peak, D. J. & Tobak, M. 1982 Three-dimensional flows about simply components at angle of attack. NASA Technical Memorandum 84226.

Ramaprian, B. R., Patel, V. C. & Choi, D. H. 1981 Mean flow measurements in the three-dimensional boundary layer over a body of revolution at incidence. *Journal of Fluid Mechanics* **103,** 479–504.

Rediniotis, O. K., Hoang, N. T. & Telionis, D. P. 1991, Multi-sensor investigations of Delta Wing high-alpha aerodynamics. AIAA Paper 91-0735.

Tobak, M. & Peake, D. J. 1982 Topology of two-dimensional separated flows. *Annual Review of Fluid Mechanics* **14,** 61–85.

Tobak, M. & Peake, D. J. 1979 Topology of two-dimensional and three-dimensional separated flows. AIAA Paper 79-1480.

Wang, K. C. 1975 Boundary layers over a blunt body at low incidence with circumferential reversed flow. *Journal of Fluid Mechanics* **72,** 49–65.

Wang, K. C. & Hsieh, T. 1992 Separation patterns and flow structures about a hemisphere-cylinder at high incidence. AIAA Paper 92-2712.

Werlé, H. 1962 Separation of axisymmetric bodies at low speed. *La Recherche Aero* **90,** 3–14.

Ying, S. X., Steger, J. L., Schiff, L. B. & Baganoff, D. 1986 Numerical simulation of unsteady viscous, high-angle-of-attack flows using a partially flux-split algorithm. AIAA Paper 86-2179.

Ying, S. X., Schiff, L. B. & Steger, J. L. 1987 A numerical study of three-dimensional separated flow past a hemisphere cylinder. AIAA Paper 87-1207.

Zilliac, G. G., Degani, D. & Tobak, M. 1990 Asymmetric vortices on a slender body of revolution. AIAA Paper 90-0388.

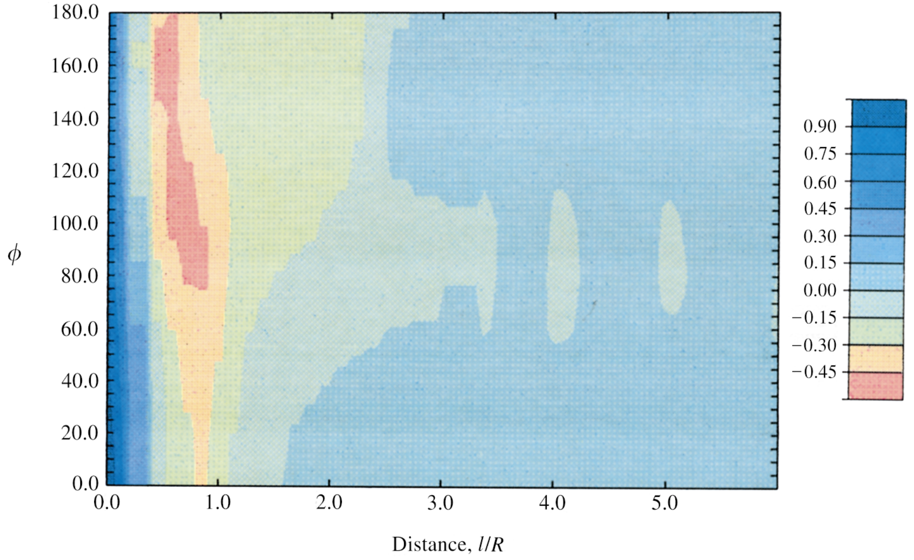

Figure 14. Pressure coefficient contours on a hemisphere-cylinder at $\alpha = 10^\circ$ and $\mathrm{Re} = 15\,000$.

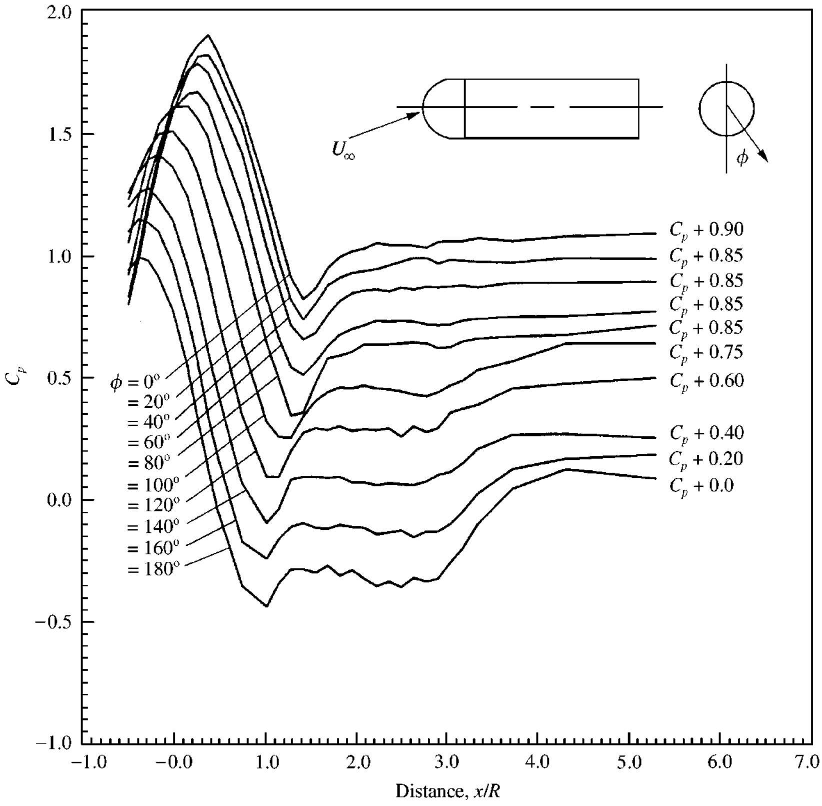

Figure 15. Axial pressure distributions on a hemisphere-cylinder at $\alpha = 20^\circ$ and $\mathrm{Re} = 15\,000$ with added constants.

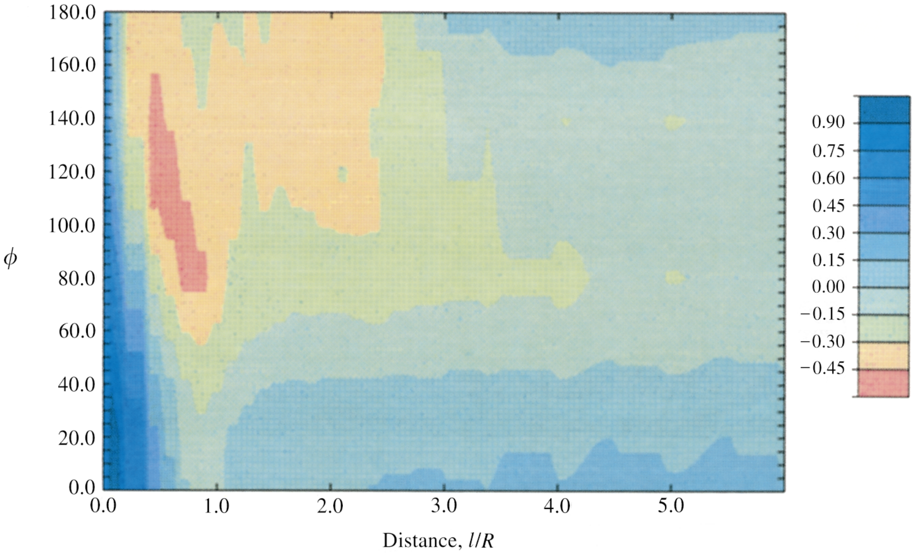

Figure 16. Pressure coefficient contours on a hemisphere-cylinder at $\alpha = 20^\circ$ and Re = 15 000

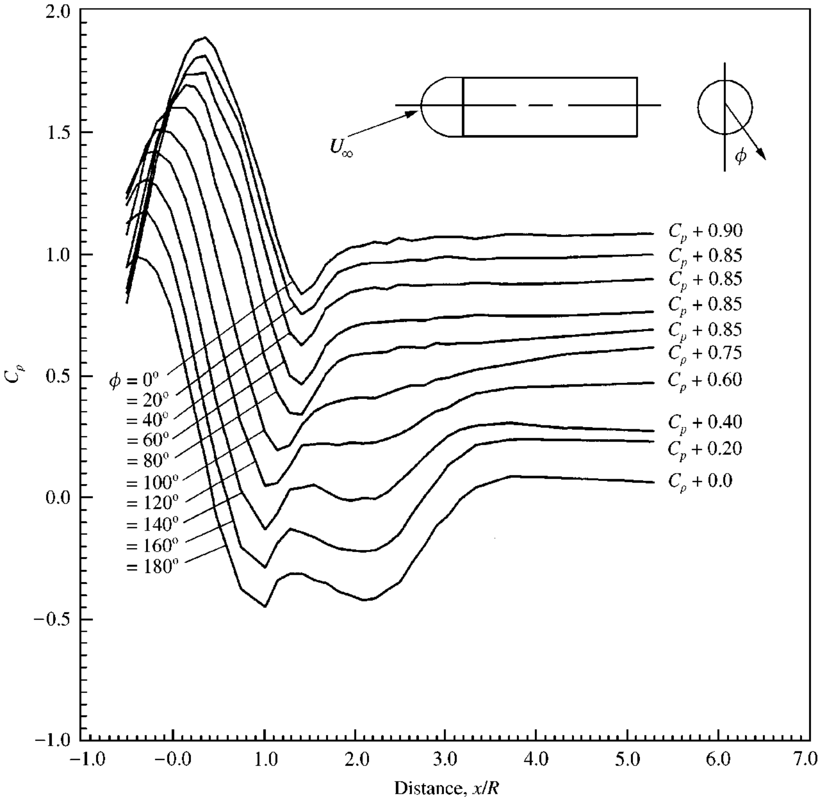

Figure 17. Axial pressure distributions on a hemisphereF-cylinder at $\alpha = 20^\circ$ and Re = 27 000 with added constants.

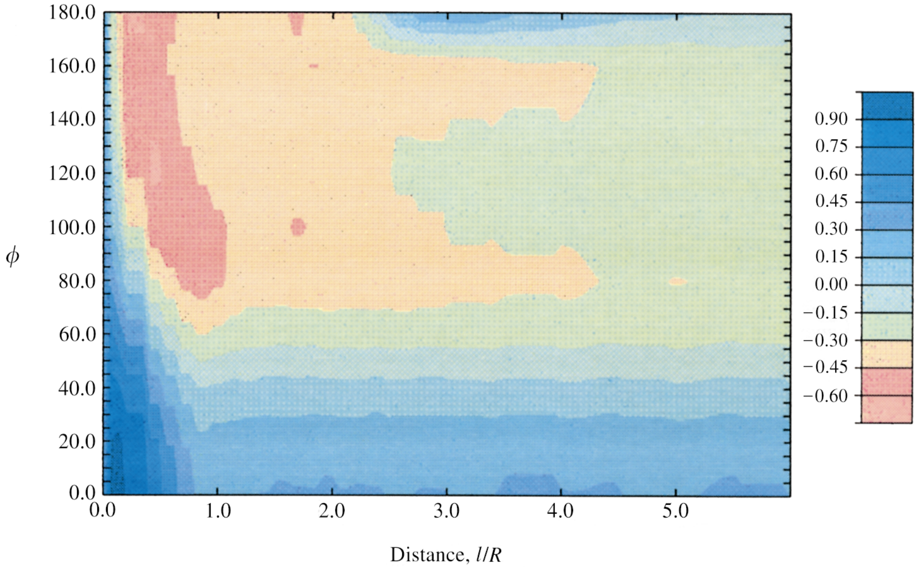

Figure 18. Pressure coefficient contours on a hemisphere-cylinder at $\alpha = 30^\circ$ and $\text{Re} = 15\,000$.

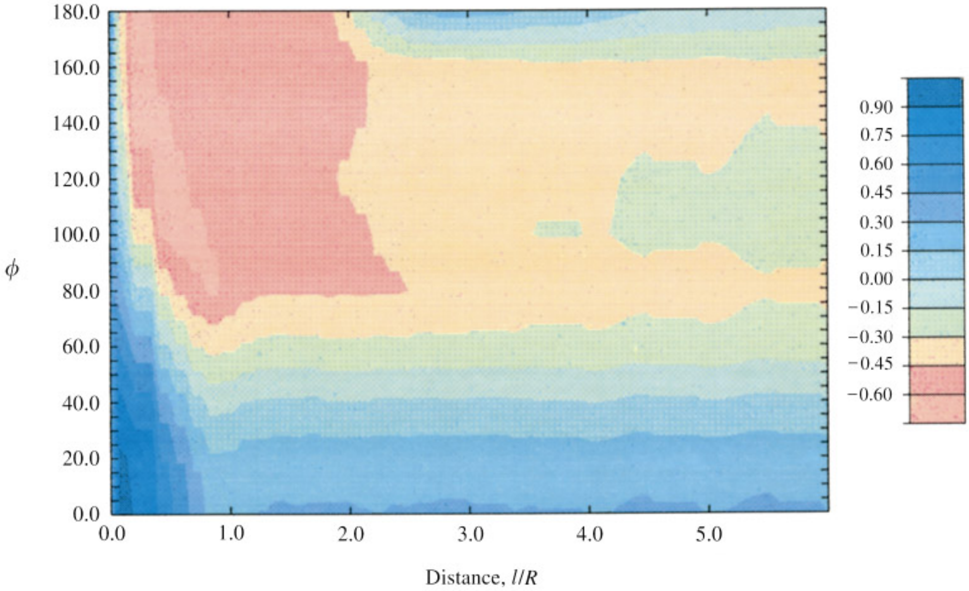

Figure 20. Pressure coefficient contours on a hemisphere-cylinder at $\alpha = 30^\circ$ and $\text{Re} = 27\,000$.

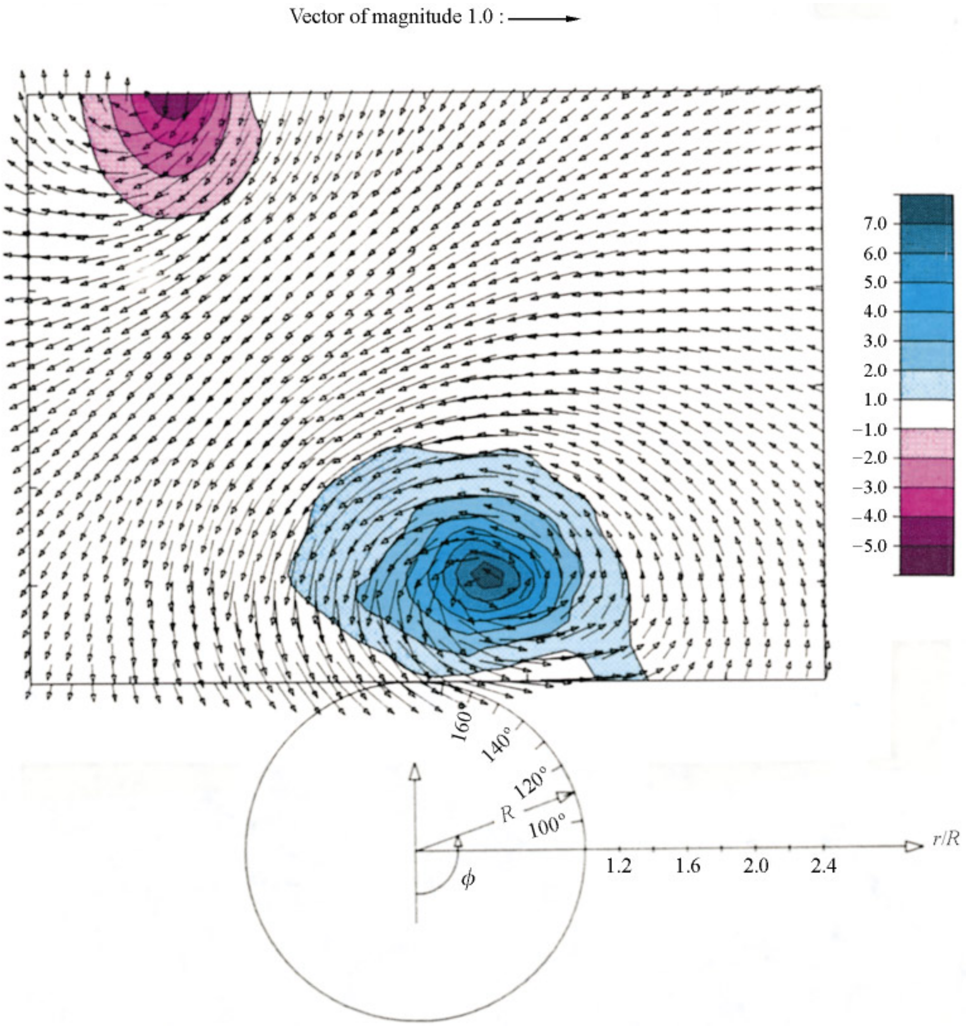

Figure 24. Velocity field and vorticity contours at $\alpha = 30^\circ$ and Re = 27 000 with bead#1 at $\phi = 120^\circ$ and $x/R = 0{\cdot}5$.

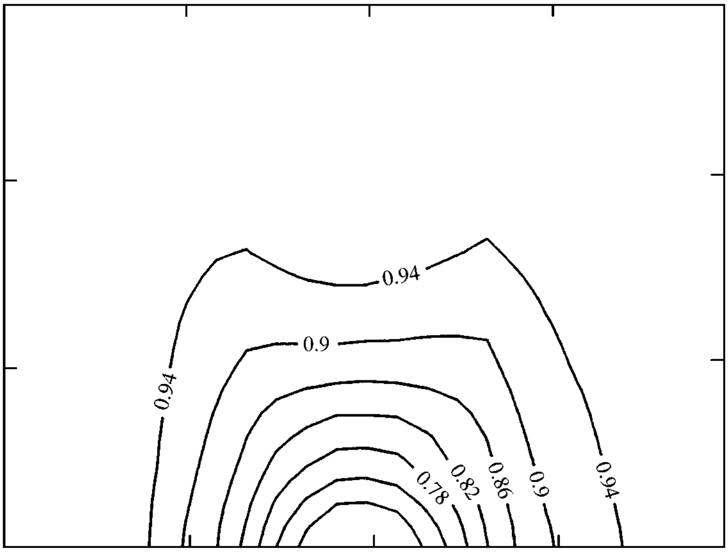

Figure 25. Axial velocity component contours at $\alpha = 30^\circ$ and Re = 27 000 with bead # 1 at $\theta = 120^\circ$ and $x/R = 0{\cdot}5$.

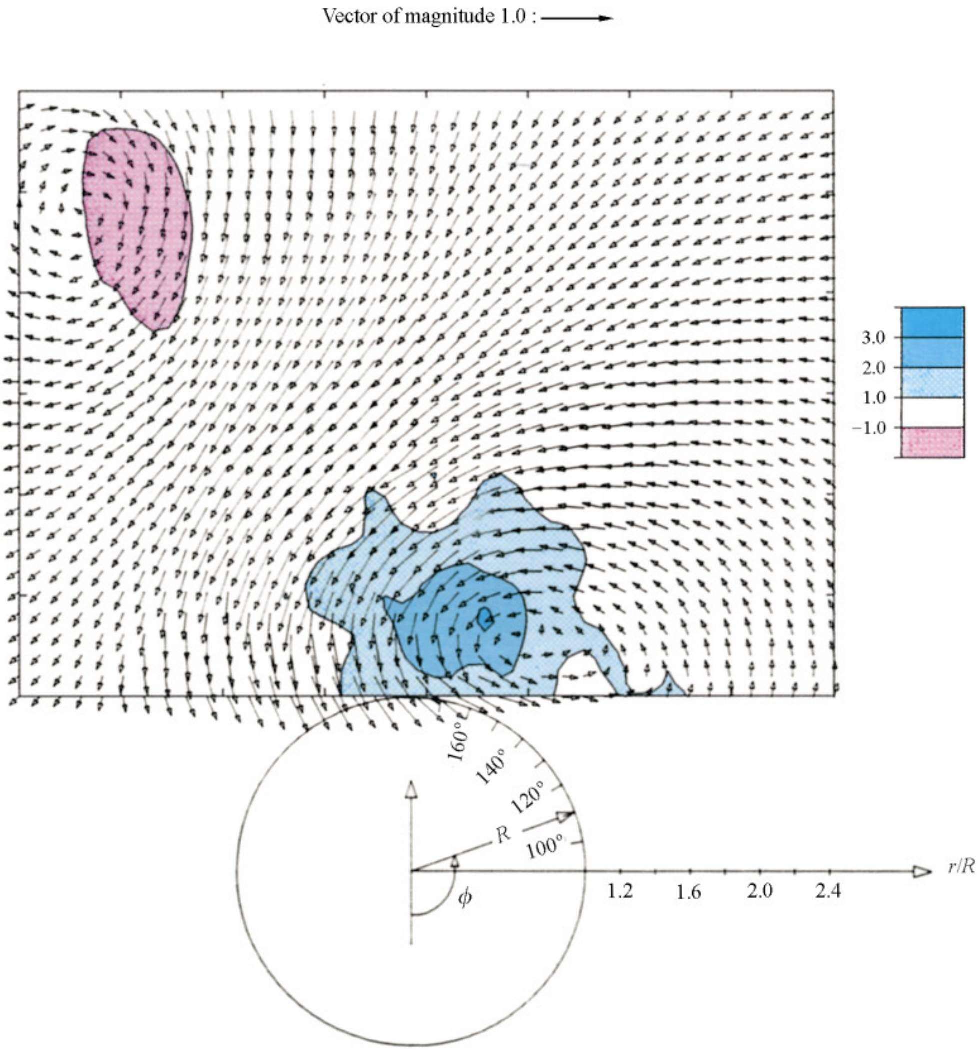

Figure 26. Velocity field and vorticity contours at $\alpha = 30^\circ$ and Re = 27 000 with bead # 1 at $\phi = 120^\circ$ and $x/R = 1{\cdot}8$.